POLITECNICO DI TORINO

Master's Degree in Aerospace Engineering

Master's Degree Thesis

# Low-thrust Earth-Moon Transfer Trajectories Optimisation via Indirect Methods

**Supervisors**
Prof. Manuela Battipede
Prof. Luigi Mascolo

**Candidate**
Edoardo Giordano

Academic Year 2025-2026

*Ai miei genitori*
*A mia sorella Alice*

# Abstract

In the last years the Moon has been in the interests of Space Economy, both for commercial and scientific purposes. More and more projects and missions concerning our natural satellite are designed and, therefore, low-cost transfers are required in the current environment.

This thesis focuses on low-thrust Earth-Moon transfer trajectories, that use electric propulsion, key of this new space exploration phase. In particular, the research is based on a three-body model, the Circular Restricted Three-Body Problem, chosen because of its accuracy with respect to others, like the Two-Body Problem. In addition, it provides the tools to understand the nuances and the complexity of the dynamics in the binary system. Moreover, within this domain, the optimisation aims to minimise the propellant usage, and it is performed via indirect methods based on optimal control theory. These methods provide very accurate solutions, usually with a minimal computational cost, despite being very sensitive to the initial conditions and difficult to converge. The formulated problem is a multipoint boundary value problem, solved with a single-shooting procedure whose control law is a *bang-bang* type: thrust is controlled by a particular function, that suggests when to fire according to its sign.

In conclusion, the research has led to the design of some optimal transfer trajectories to the Moon, plausible for scientific unmanned missions. These results mark the basis for further analysis that can explore the optimisation of low-energy trajectories for the binary system. Some numerical solutions are, therefore, added to a problem that has been studied for centuries and that is still in the interest of engineers, physicists and mathematicians.

# Contents

# List of Figures

# List of Tables

# Acronyms

| | |
|---|---|
| 2BP | Two-Body Problem. |
| 3BP | Three-Body Problem. |
| BC | Boundary Condition. |
| BVP | Boundary Value Problem. |
| CR3BP | Circular Restricted Three-Body Problem. |
| CoM | Centre of Mass. |
| EP | Electric Propulsion. |
| EoM | Equations of Motion. |
| IM | Indirect Method. |
| LEO | Low Earth Orbit. |
| LP | Lagrangian Point. |
| MPBVP | Multi-Point Boundary Value Problem. |
| OCP | Optimal Control Problem. |
| ODE | Ordinary Differential Equation. |
| PMP | Pontryagin's Maximum Principle. |
| RF | Reference Frame. |
| SC | Spacecraft. |
| SF | Switching Function. |
| TPBVP | Two Points Boundary Value Problem. |

# 1 | Introduction

## 1.1 Preface

The Moon has always been an integral part of human history. As the brightest object in the night sky, its rhythmic phases provided the first fundamental unit of time, serving as a celestial clock and calendar for ancient civilizations. Its presence in our firmament led to the birth of myths, poems, and paintings across the world; we observed the Moon and imagined it as a divinity. For the Greeks, it was Artemis or Selene for the Chinese, the lunar deity Chang'e and for the Norse, Máni. Regardless of the name, these cultures were all looking at the same silent companion.

This perception shifted dramatically with the advent of the telescope. In 1609, the astronomer, physicist, and philosopher Galileo Galilei pointed his lens toward the Moon and revealed its true identity: not a perfect, ethereal sphere, but a rugged, imperfect celestial body dotted with mountains and valleys. Galileo's detailed sketches (Figure 1.1) marked the birth of lunar topography.

Following Galileo, the study of the Moon's behaviour became a primary challenge for classical mechanics. Following Kepler's initial speculations on its motion, Isaac Newton provided the first gravitational description of the Earth-Moon system through his law of universal gravitation. Later, 18th and 19th-century scholars like Euler and Lagrange developed the foundational theories of the *Three-Body Problem*, to model the intricate orbital dynamics of our satellite.

The great turning point arrived in the 20th century. While the dream of a lunar journey was omnipresent, technology had yet to catch up with imagination. In 1902, Georges Méliès released *Voyage dans la Lune* (Figure 1.2), a film based on Jules Verne's 1865 novel *De la Terre à la Lune, trajet direct en 97 heures 20 minutes*, where a bizarre adventure to the Moon is illustrated.

On July 20, 1969, that science-fiction dream became reality. When American astronaut Neil Armstrong stepped onto the lunar soil, the human species became truly interplanetary. The Apollo 11 mission was a monumental success

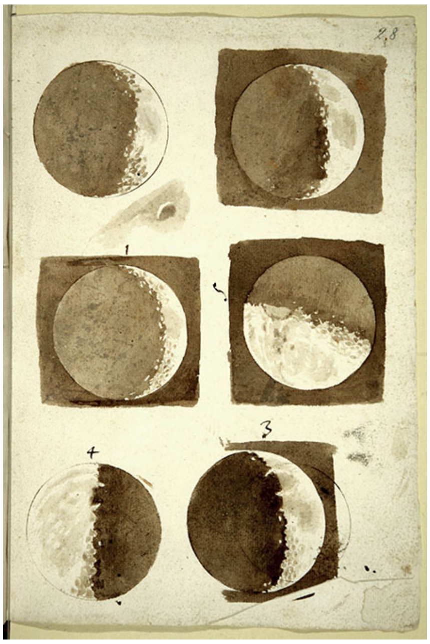

Figure 1.1: *Drawings of the Moon*, November-December 1609 [1]

of engineering, shaped by the intense geopolitical pressure of the Cold War. Five more successful landings followed, but by December 1972, with the conclusion of Apollo 17, no human has since returned to set foot upon the lunar soil. For decades, the lunar surface remained silent, waiting for a new era of orbital mechanics and renewed ambition to bridge the gap once again.

## 1.2 Lunar Renaissance

The turn of the century has marked a revitalised global interest in the Moon, a scenario often called *Lunar Renaissance* [2]. Unlike the politically charged Space Race of the 1960s, the current era is defined by a collaborative and commercial landscape involving both national space agencies and private enterprises. This shift reflects a move away from the high-risk, frenetic pace of the past toward a more measured approach that prioritises scientific longevity and the development of a lunar economy. While the frequency of missions may be lower than during the Space Race peak, the emphasis on risk mitigation has led to higher success rates and a sustainable roadmap for returning humans to the lunar surface.

Scientific objectives remain the primary catalyst for modern lunar exploration. Over the last two decades, dozens of missions have successfully mapped the lunar surface and analysed soils composition. A notable milestone was the ESA's SMART-1 mission (2003) [3], which served a dual purpose: it was the

Figure 1.2: A frame of "*Voyage dans la Lune*", Georges Méliès, 1902

first European spacecraft to reach the Moon, and it successfully demonstrated the use of ion thrusters for lunar transfers. Furthermore, its X-ray spectrometer provided critical data on surface mapping. This era also saw significant contributions from Japan, India, and the United States, culminating in China's Chang'e 3 mission in 2013 [4]. This marked the first soft landing on the Moon since the Soviet Union's Luna 24 in 1976, deploying the Yutu rover to explore the Mare Imbrium region.

Modern lunar exploration has expanded its scope; while scientific research remains a fundamental pillar, the focus now includes the pursuit of a sustained human presence and in-situ resource utilisation. These objectives are deeply interconnected, as the search for water ice and the deployment of radio astronomy arrays on the lunar far side represent both scientific frontiers and economic catalysts. Central to this effort is NASA's Artemis program [5], which is working to bring humanity back to the Moon and establish a permanent base camp. This is being achieved through a phased approach designed to test new technologies and study human physiology in deep space. Simultaneously, a global landscape of institutional and private actors has emerged: Denmark's Máni mission aims for high-resolution surface mapping, while China's Chang'e 7 utilises a complex architecture to prospect for polar ice. Furthermore, commercial ventures like the second Blue Ghost mission will capitalise on the "radio silence" of the lunar far side to establish a new vantage point for deep-space radio astronomy.

Within this framework, the present thesis proposes the computation of optimal transfer trajectories to access the lunar environment and insert a spacecraft into a stable orbit for further mission operations. Specifically, the objective is to minimise fuel consumption, offering more payload capacity. To capture the complex gravitational dynamics of the Earth-Moon system, the trajectories are modelled in the Circular Restricted Three-Body Problem, a medium-fidelity framework that accounts for the simultaneous gravitational influence of both primary bodies.

## 1.3 Main objectives

As previously discussed, the Moon holds significant scientific and engineering value, making Earth-Moon trajectory design the subject of extensive research. Historically, various dynamical models have been employed based on the required fidelity and specific mission constraints. Within the framework of the Two-Body Problem, the direct transfer, modeled via Hohmann transfers or the patched-conics method remains the most straightforward approach. This was the preferred strategy for missions ranging from Apollo to Chang'e, as it prioritises short flight times, albeit at the cost of high-energy requirements. Conversely, by incorporating the Sun's gravitational influence into the binary system, low-energy transfers can be computed. These trajectories significantly reduce propellant consumption by leveraging ballistic capture, though they necessitate substantially longer flight times. A comprehensive review of these transfer strategies is provided in [6].

The primary objective of this thesis is the computation of mass-efficient transfer trajectories. To achieve this, Electric Propulsion was selected due to its high specific impulse, making it suited for high-$\Delta V$ missions. To capture the complex gravitational nuances of the Earth-Moon system, a medium-fidelity dynamical framework was adopted. Specifically, the spacecraft's equations of motion are integrated within the Circular Restricted Three-Body Problem, allowing for a more accurate representation of the third-body effects that are neglected in traditional patched-conic approximations.

Consequently, the optimisation objective focuses on maximising the final spacecraft mass by minimising propellant consumption. To solve this, the Optimal Control Problem is defined using an indirect formulation. This approach transforms the OCP into a Boundary Value Problem by applying optimality conditions, providing the mathematical rigour necessary to guarantee an optimal solution.

In this context, the primary objectives of this thesis are:

- To derive and define a Boundary Value Problem for low-thrust trajectories using indirect methods;
- To implement a single-shooting numerical method to solve the resulting Boundary Value Problem;
- To obtain and analyse optimal transfer solutions that achieve spacecraft insertion into a stable lunar orbit.

## 1.4 Thesis overview

The structure of this thesis is organised as follows.

Chapter 2 establishes the foundational methodology used throughout the research. It begins with a definition of the Two-Body Problem, followed by an extensive analysis of the Circular Restricted Three-Body Problem. Key dynamical features are explored, including the derivation of the equations of motion, the Jacobi integral, and the determination of Zero-Velocity Surfaces. The chapter concludes with a characterization of the Earth-Moon system and an introduction to the performance of electric propulsion systems.

Chapter 3 focuses on the theoretical framework of Optimal Control Theory. A comparative overview of direct and indirect optimisation methods is provided, leading into a detailed derivation of the indirect formulation. By applying optimality conditions, the Optimal Control Problem is transformed into a Boundary Value Problem. The chapter then details the implementation of the single-shooting method used to solve the system and illustrates the specific OCP configuration tailored for this research.

Chapter 4 presents the numerical results of the study. A baseline Earth-Moon transfer trajectory is first computed and discussed. Subsequently, two distinct orbital solutions are analysed, highlighting the impact of different switching structures.

The final chapter provides a comprehensive summary of the research.

# 2 | Methodology

This chapter outlines the methodology employed throughout this research.

First, the Two-Body Problem is established. The model is derived from fundamental principles, defining the necessary reference frames and equations of motion. Subsequently, the higher-fidelity Three-Body Problem is discussed in detail. Starting from the general formulation, specific constraints are applied to derive the Circular Restricted Three-Body Problem, which serves as the primary framework for this work. Within this domain, the Jacobi integral, Lagrange points, and Zero-Velocity Surfaces are analysed. A brief overview of the Earth-Moon system follows, providing the specific parameters used in this study. Finally, the performance characteristics of Electric Propulsion are introduced to contextualise the propulsive systems under consideration.

The following notation is used throughout this thesis: vectors are denoted by lowercase bold fonts ($\boldsymbol{x}$), with the exception of known quantities like velocity ($\boldsymbol{V}$) and thrust ($\boldsymbol{T}$). Unit vectors are indicated by a hat ($\hat{\boldsymbol{x}}$), while matrices are represented by uppercase bold letters ($\mathbf{J}$). First and higher-order time derivatives are denoted by single or multiple dots, respectively ($\dot{x}, \ddot{x}$). To maintain clarity between physical and normalized domains, non-dimensional quantities are presented using Greek letters (e.g., $\xi$) or calligraphic fonts (e.g., $\mathcal{U}$), unless otherwise specified.

## 2.1 Two-body problem

The motion of a spacecraft is shaped, at any given instant, by gravitational forces from celestial bodies. These forces were described for the first time by the English mathematician Isaac Newton, in his book *Principia* (1687), and are the foundation of space flight dynamics. Newton's law of universal gravitation can be expressed as follows:

$$F = G\,\frac{m_1 \cdot m_2}{r^2} \tag{2.1}$$

where $G$ is the universal constant, $m_1$ and $m_2$ the mass of the two bodies and $r$ their relative distance.

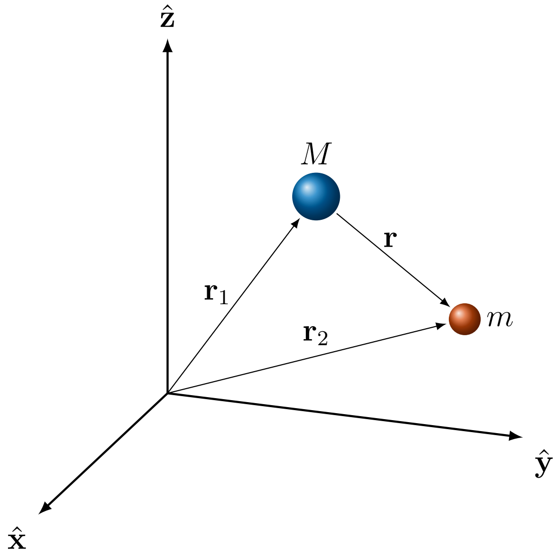

Figure 2.1: Two-Body Problem

Applying Newton's second law of motion to the spacecraft mass ($m_2$) in a generic N-body system, it yields:

$$m_2 \cdot \ddot{\mathbf{r}}_2 = \sum_{\substack{j=1 \\ j\neq 2}}^{N} \mathbf{F}_{2j} \tag{2.2}$$

From such complex systems it is not possible to obtain an analytical solution and, in order to find the motion of the spacecraft, numerical integration is required.

In case only two masses are considered (Figure 2.1), the model takes the name of Two-Body Problem (2BP): it simplifies the complexity due to multi-body interactions and provides an elegant analytical solution.

The assumptions for the 2BP, also known as *Kepler's problem*, are [7]:

- The two bodies are spherically symmetric so that they may be considered as particles or point masses;
- The mutually attractive gravitational forces are the only forces acting in the two-body system;
- The mass $m$ is negligible compared with $M$.

From Equations (2.1) and (2.2), considering the relative position vector

$\mathbf{r} = \mathbf{r}_2 - \mathbf{r}_1$ in an inertial reference frame, one can find:

$$\ddot{\mathbf{r}} = -G\,\frac{M+m}{\mathbf{r}^3}\mathbf{r} \tag{2.3}$$

and, since $M \gg m$, Equation (2.3) becomes

$$\ddot{\mathbf{r}} \approx -G\,\frac{M}{\mathbf{r}^3}\mathbf{r} = -\frac{\mu}{\mathbf{r}^3}\mathbf{r} \tag{2.4}$$

where $\mu = G \cdot M$ is the planetary gravitational parameter. Useful $\mu$ values for the present thesis are provided in Table (2.1). The Equations of Motion (EoM) can be now easily obtained:

$$\ddot{\mathbf{r}} + \frac{\mu}{\mathbf{r}^3}\mathbf{r} = \mathbf{0} \tag{2.5}$$

| Body | $\mu$ [km$^3$/s$^2$] |
|---|---|
| Earth | $3.98600 \cdot 10^5$ |
| Moon | $4.90280 \cdot 10^3$ |
| Sun | $1.32712 \cdot 10^{11}$ |

Table 2.1: Gravitational parameter for Earth, Moon and Sun [8].

Behind the analytical solution of the 2BP stand two constants of motion. The first quantity is the specific mechanical energy $\mathcal{E}$, defined by the *vis-viva* equation:

$$\mathcal{E} = \frac{V^2}{2} - \frac{\mu}{r} \tag{2.6}$$

This specific energy is composed by a kinetic term ($V^2/2$) and a potential one ($\mu/r$): such quantity, in the domain of a Keplerian orbit, remains constant.

The second law of conservation regards the specific angular momentum:

$$\mathbf{h} = \mathbf{r} \times \mathbf{V} \tag{2.7}$$

and because $\mathbf{h}$ is constant, the orbital plane is fixed in the space.

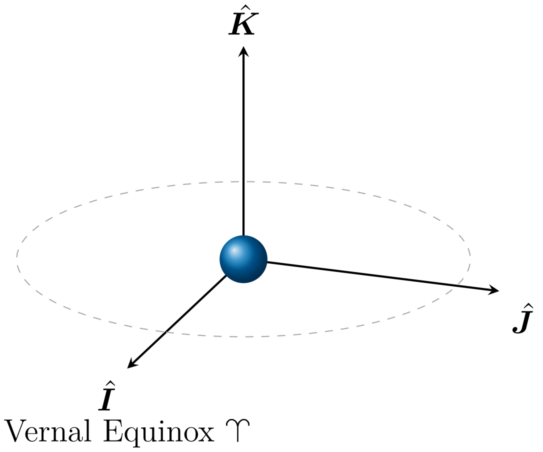

Figure 2.2: EME2000 Reference Frame

### 2.1.1 EME2000 reference system

In order to apply Newton's laws of dynamics, an inertial Reference Frame (RF) is required. A generic RF is defined by a triad of orthonormal vectors oriented in space and can be classified into two types: inertial and non-inertial. The first ones do not accelerate and do not rotate, and it is possible to apply Newton's laws; in the others apparent accelerations such as tangential, Coriolis and centrifugal ones appear. The choice of the RF depends on the problem: in some cases the use of a rotating RF can be useful to simplify the equations at stake.

For the 2BP one of the most common is the Earth's Mean Equator and Mean Equinox, or EME2000, a quasi-inertial geocentric-equatorial coordinate system (Figure 2.2). Its origin is located in the centre of the Earth, while the fundamental plane lays on the equatorial one. The unit vectors are oriented as follows: $\hat{\boldsymbol{I}}$ points the vernal equinox direction, described by the symbol of the constellation Aries $\Upsilon$, $\hat{\boldsymbol{K}}$ is perpendicular to the fundamental plane and $\hat{\boldsymbol{J}}$ completes the right-hand triad [7].

To facilitate the satellite's motion description, the EME2000 can be lined with two more RFs. The first is the non-inertial perifocal RF $\{\hat{\boldsymbol{p}}_{SC},\ \hat{\boldsymbol{q}}_{SC},\ \hat{\boldsymbol{r}}_{SC}\}$, whose fundamental plane is the orbital one. The $\hat{\boldsymbol{p}}_{SC}$ axis is aligned with the eccentricity vector $\boldsymbol{e}$, $\hat{\boldsymbol{q}}_{SC}$ with the specific angular momentum $\boldsymbol{h}$ and $\hat{\boldsymbol{r}}_{SC}$ completes the triad. The second is the non-inertial Zenith-East-North (ZEN) RF $\{\hat{\boldsymbol{u}},\ \hat{\boldsymbol{v}},\ \hat{\boldsymbol{w}}\}$, attached to the Spacecraft (SC)'s position vector with respect to the Earth. Specifically, the $\hat{\boldsymbol{u}}$ axis is aligned with the radius $r$ (from witch 'radial' direction), $\hat{\boldsymbol{v}}$ perpendicular to it, pointing the direction of motion, and $\hat{\boldsymbol{w}}$ completes the triad, pointing the North pole within the orbital plane.

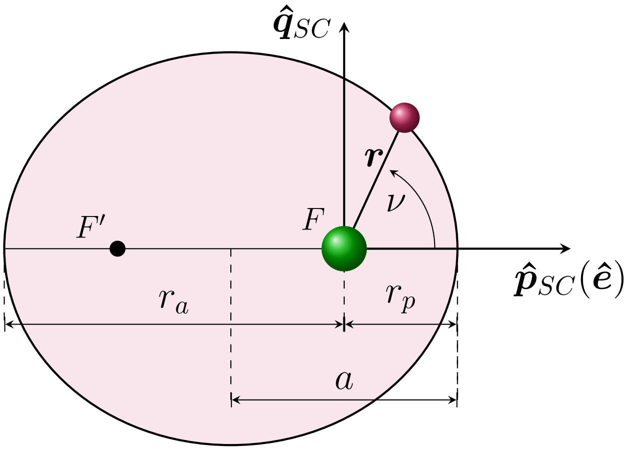

Figure 2.3: Perifocal Reference Frame

### 2.1.2 Conic equation

Considering a closed unperturbed orbit, a SC would follow a specified path, according to Kepler's laws. This trajectory can be uniquely characterised by a set of six parameters {a, e, i, $\Omega$, $\omega$, $\nu$}, called Keplerian elements, that define the orbital geometry and its orientation in space. The semi-major axis $a$ represents the orbit's dimension, while the eccentricity $e$ determines the shape. Specifically, a null eccentricity corresponds to a circular orbit, while a value below the unity defines an ellipse; values over the unity describe more energetic parabolic ($e = 1$) and hyperbolic trajectories ($e > 1$).

For an elliptical orbit, the SC would transition from the closest point above the planet's surface, the *periapsis*, and the furthest, the *apoapsis*. Its position on the perifocal RF is uniquely defined by $\nu$, the angle between the spacecraft's position vector $r$ and the vector planet-periapsis. These three parameters compose the well-known *conic equation*

$$r = \frac{a(1 - e^2)}{1 + e\cos\nu} \tag{2.8}$$

To orient the orbit in space, with respect to EME2000 RF, the remaining three Keplerian elements are employed. The inclination $i$ measures the angle between the orbital and equatorial planes. Their intersection generates the line of nodes $\boldsymbol{n}$, a segment that states the passage from the southern to northern hemisphere; the right ascension of the ascending node (RAAN) $\Omega$ locates this line with respect to the $\hat{\boldsymbol{I}}$ axis. Finally, $\omega$ is the *argument of periapsis* and specifies where is located the periapsis with respect to the line of nodes. All the elements on the perifocal RF are illustrated in Figure (2.3).

## 2.2 Three-body problem

Adding another celestial body to the model, it takes the name of Three-Body Problem (3BP). This model increases the fidelity of the problem, especially where the spacecraft is considerably affected by both celestial bodies: the trajectories are shaped by the gravitational force of both, but, despite the 2BP, this model denies a closed-form solution.

However, making a couple of assumptions, the 3BP gives some analytical expressions useful to manipulate the problem, while protecting its complexity. In fact, two main gravitational bodies are considered (e.g. Earth and Moon), called the *primaries*, and one smaller object, the spacecraft. The required assumptions are:

- the two gravitational bodies move in circular orbits around their Centre of Mass (CoM);
- the mass of the third body is negligible and does not influence the motion of the primaries.

The model is the so-called Circular Restricted Three-Body Problem (CR3BP). A consequence of the first assumption is that the mass of the SC must be null: a mass not equal to zero would compromise the planar motion of the primaries and would violate the conservation of energy and angular momentum [7, 9]. However, considering the second assumption, the planarity is a good approximation.

Since the motion of the celestial bodies is known, the problem is to determine the motion of the third body, the spacecraft.

To represent this problem, two RFs can be used (Figure 2.4). The first, $\{\hat{\boldsymbol{X}}_F, \hat{\boldsymbol{Y}}_F, \hat{\boldsymbol{Z}}_F\}$, is an inertial RF, with origin $\mathcal{O}$ on the binary system's CoM: the $\hat{\boldsymbol{Z}}_F$-axis is perpendicular to the plane of motion of the primaries. On the other hand, $\{\hat{\boldsymbol{x}}_S, \hat{\boldsymbol{y}}_S, \hat{\boldsymbol{z}}_S\}$ is the *synodic* RF, non inertial, that rotates with respect to the other with an angular velocity $\omega_S(t)$: the $\hat{\boldsymbol{x}}_S$-axis is in the direction that links the primaries, towards the smaller mass, $\hat{\boldsymbol{z}}_S$ parallel to $\hat{\boldsymbol{Z}}_F$ and $\hat{\boldsymbol{y}}_S$ completes the triad. So the two RFs share the same fundamental plane and origin, and the SC is free to move in the tree-dimensional space they define.

The angular velocity $\omega_S(t)$ depends on the distance between the primaries, $\mathbf{r}_{12}$. Defining the relative distance vector between two bodies

$$\mathbf{r}_{ij}(t) = \mathbf{r}_j(t) - \mathbf{r}_i(t) \tag{2.9}$$

and the absolute distance vector, with respect to the origin $\mathcal{O}$

$$\mathbf{r}_{\mathcal{O}j}(t) = \mathbf{r}_j(t) \tag{2.10}$$

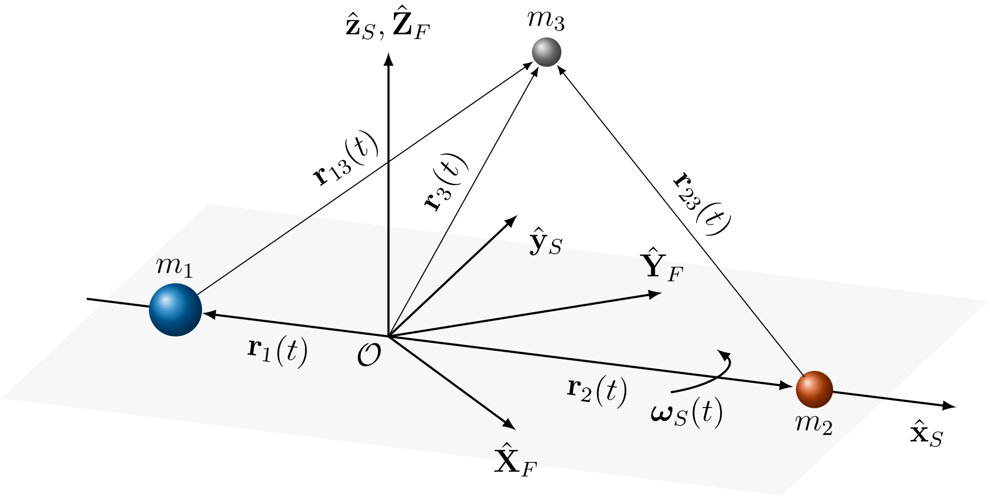

Figure 2.4: Inertial and synodic reference frames

the angular velocity can be expressed as follows:

$$\omega_S(t) = \sqrt{G\,\frac{m_1 + m_2}{\mathbf{r}_{12}^3(t)}} \tag{2.11}$$

where $G(m_1 + m_2) = \mu_1 + \mu_2 = \mu^*$.

Since the primaries move in circular orbits around $\mathcal{O}$, $\mathbf{r}_1$ and $\mathbf{r_2}$ are constant (and so $\mathbf{r}_{12}$), hence the angular velocity is constant in time.

In such a problem, many quantities with very different magnitude are considered. In order to restrict their range and to help the calculators, an adimensionalisation is performed. Three characteristic values are set to match every quantity with a corresponding non-dimensional one:

$$\begin{cases} l^* = r_{12} \\ m^* = m_1 + m_2 \\ \mathcal{T}^* \triangleq \sqrt{\dfrac{{l^*}^3}{Gm^*}} \end{cases}$$

where $l^*$ is the distance between the primaries, $m^*$ the sum of their masses and $\mathcal{T}^*$ derived, so that the non-dimensional universal gravitational constant is equal to the unity in Kepler's third law.

From these three characteristic values, some useful non-dimensional quantities can be obtained:

$$\begin{cases} \rho_{12} = \dfrac{r_{12}}{l^*} \\ \mu = \dfrac{m_2}{m^*} \\ \tau = \dfrac{\mathcal{T}}{\mathcal{T}^*} = 2\pi \end{cases}$$

The only parameter of the system is the *mass parameter* $\mu$. Assuming $m_1 > m_2$, then $\mu \in [0, \frac{1}{2}]$ and the non-dimensional masses of the primaries become, respectively

$$\mu_1 = 1 - \mu \tag{2.12a}$$

$$\mu_2 = \mu \tag{2.12b}$$

This parameter determines the type of motion possible for the spacecraft, assuming an analogy with Reynold's number $Re$ in fluid mechanics [10].

After some mathematical manipulations, one can find the barycentre's distance with respect to the bigger celestial body

$$\rho_{CG} = \frac{\sum_i \rho_i \mu_i}{\sum_i \mu_i} = \mu \tag{2.13}$$

from which

$$\rho_1 = \frac{r_1}{l^*} = -\mu \tag{2.14a}$$

$$\rho_2 = \frac{r_2}{l^*} = 1 - \mu \tag{2.14b}$$

### 2.2.1 Equations of motion

By applying Newton's second law to this system, the spacecraft's acceleration can be expressed as

$$\ddot{\mathbf{r}} = -\frac{\mu_1}{r_{13}^2}\frac{\mathbf{r}_{13}}{r_{13}} - \frac{\mu_2}{r_{23}^2}\frac{\mathbf{r}_{23}}{r_{23}} \tag{2.15}$$

Projecting this acceleration on the three directions of the synodic RF, one has

$$\ddot{\mathbf{x}} = -\frac{\mu_1}{r_{13}^3}(x - x_1) - \frac{\mu_2}{r_{23}^3}(x - x_2) \tag{2.16a}$$

$$\ddot{\mathbf{y}} = -\frac{\mu_1}{r_{13}^3}y - \frac{\mu_2}{r_{23}^3}y \tag{2.16b}$$

$$\ddot{\mathbf{z}} = -\frac{\mu_1}{r_{13}^3}z - \frac{\mu_2}{r_{23}^3}z \tag{2.16c}$$

where $r_{i3}$ are the relative position vectors, defined as

$$r_{i3} = \sqrt{(x - x_i)^2 + y^2 + z^2}, \qquad i = 1, 2 \tag{2.17}$$

It is useful to project these EoM in an inertial RF such as $(\hat{\boldsymbol{X}}_F, \hat{\mathbf{Y}}_F, \hat{\boldsymbol{Z}}_F)$. In order to do so, the *transport theorem* is used; for a generic quantity *, it states

$$\frac{d*}{dt} = \frac{\delta *}{\delta t} + \boldsymbol{\omega}_{R/F} \times * \tag{2.18}$$

where $d/dt$ refers to the quantity in the inertial reference frame, $\delta/\delta t$ in the rotating one and $\boldsymbol{\omega}$ is the angular velocity calculated in the rotating reference frame with respect to the inertial one.
From Equation (2.18) it is possible to obtain the velocity of the spacecraft in the inertial frame

$$\dot{\mathbf{r}}_F = \frac{d\mathbf{r}}{dt} = \frac{\delta \mathbf{r}}{\delta t} + \boldsymbol{\omega}_S \times \mathbf{r} \tag{2.19}$$

and, thus, the acceleration

$$\begin{aligned}
\ddot{\mathbf{r}}_F &= \frac{d^2\mathbf{r}}{dt^2} \\
&= \frac{\delta}{\delta t}\left(\frac{d\mathbf{r}}{dt}\right) + \boldsymbol{\omega}_S \times \frac{d\mathbf{r}}{dt} \\
&= \frac{\delta}{\delta t}\left(\dot{\mathbf{r}} + \boldsymbol{\omega}_S \times \mathbf{r}\right) + \boldsymbol{\omega}_S \times \left(\dot{\mathbf{r}} + \boldsymbol{\omega}_S \times \mathbf{r}\right) \\
&= \ddot{\mathbf{r}} + \dot{\boldsymbol{\omega}}_S \times \mathbf{r} + 2\boldsymbol{\omega}_S \times \dot{\mathbf{r}} + \boldsymbol{\omega}_S \times \left(\boldsymbol{\omega}_S \times \mathbf{r}\right)
\end{aligned} \tag{2.20}$$

where in the last line all the terms are referred to the rotating RF and

$$\boldsymbol{\omega}_S = \omega_S \hat{\boldsymbol{z}}_S \tag{2.21}$$

The first term in the right-hand side of Equation (2.20) is the acceleration of the third body in the synodic RF, while the other three are, respectively, tangential, centripetal and Coriolis accelerations. From Equation (2.11), and considering the assumptions of the CR3BP, one can see that the angular velocity is constant in time, hence the tangential term is null in this case

$$\ddot{\mathbf{r}}_F = \ddot{\mathbf{r}} + 2\boldsymbol{\omega}_S \times \dot{\mathbf{r}} + \boldsymbol{\omega}_S \times (\boldsymbol{\omega}_S \times \mathbf{r}) \tag{2.22}$$

With these considerations, one can expand Equation (2.19) and find the components of inertial velocity

$$\begin{aligned}\dot{\mathbf{r}}_F &= (\dot{x}\hat{\boldsymbol{x}}_S + \dot{y}\hat{\boldsymbol{y}}_S + \dot{z}\hat{\boldsymbol{z}}_S) + \begin{vmatrix} \hat{\boldsymbol{x}}_S & \hat{\boldsymbol{y}}_S & \hat{\boldsymbol{z}}_S \\ 0 & 0 & \omega_S \\ x & y & z \end{vmatrix} \\ &= (\dot{x}\hat{\boldsymbol{x}}_S + \dot{y}\hat{\boldsymbol{y}}_S + \dot{z}\hat{\boldsymbol{z}}_S) + (-y\omega_S)\hat{\boldsymbol{x}}_S + (x\omega_S)\hat{\boldsymbol{y}}_S + (0)\hat{\boldsymbol{z}}_S \\ &= (\dot{x} - y\omega_S)\hat{\boldsymbol{x}}_S + (\dot{y} + x\omega_S)\hat{\boldsymbol{y}}_S + (\dot{z})\hat{\boldsymbol{z}}_S \end{aligned} \tag{2.23}$$

and Equation (2.22) for the acceleration

$$\begin{aligned}\ddot{\mathbf{r}}_F &= \ddot{\mathbf{r}} + 2\begin{vmatrix} \hat{\boldsymbol{x}}_S & \hat{\boldsymbol{y}}_S & \hat{\boldsymbol{z}}_S \\ 0 & 0 & \omega_S \\ \dot{x} & \dot{y} & \dot{z} \end{vmatrix} + \boldsymbol{\omega}_S \begin{vmatrix} \hat{\boldsymbol{x}}_S & \hat{\boldsymbol{y}}_S & \hat{\boldsymbol{z}}_S \\ 0 & 0 & \omega_S \\ x & y & z \end{vmatrix} \\ &= (\ddot{x} - 2\dot{y}\omega_S)\hat{\boldsymbol{x}}_S + (\ddot{y} + 2\dot{x}\omega_S)\hat{\boldsymbol{y}}_S + (\ddot{z})\hat{\boldsymbol{z}}_S + \begin{vmatrix} \hat{\boldsymbol{x}}_S & \hat{\boldsymbol{y}}_S & \hat{\boldsymbol{z}}_S \\ 0 & 0 & \omega_S \\ -y\omega_S & x\omega_S & 0 \end{vmatrix} \\ &= (\ddot{x} - 2\dot{y}\omega_S - x\omega_S^2)\hat{\boldsymbol{x}}_S + (\ddot{y} + 2\dot{x}\omega_S - y\omega_S^2)\hat{\boldsymbol{y}}_S + (\ddot{z})\hat{\boldsymbol{z}}_S \end{aligned} \tag{2.24}$$

By equalling Equations (2.16) and (2.24) one can find the EoM in the synodic RF

$$\ddot{x} - 2\dot{y}\omega_S - x\omega_S^2 = -\frac{\mu_1}{r_{13}^3}(x - x_1) - \frac{\mu_2}{r_{23}^3}(x - x_2) \tag{2.25a}$$

$$\ddot{y} + 2\dot{x}\omega_S - y\omega_S^2 = -\frac{\mu_1}{r_{13}^3}y - \frac{\mu_2}{r_{23}^3}y \tag{2.25b}$$

$$\ddot{z} = -\frac{\mu_1}{r_{13}^3}z - \frac{\mu_2}{r_{23}^3}z \tag{2.25c}$$

Furthermore, by applying the non-dimensionalisation, the angular velocity becomes $\omega_S = 1$, so $\dot{\omega}_S = 0$ and the full non-dimentional set of Ordinary Differential Equations (ODEs) in cartesian components for the CR3BP are obtained

$$\ddot{\xi} - 2\dot{\eta} - \xi = -\frac{1-\mu}{\rho_{13}^3}(\xi + \mu) - \frac{\mu}{\rho_{23}^3}[\xi - (1-\mu)] \tag{2.26a}$$

$$\ddot{\eta} + 2\dot{\xi} - \eta = -\frac{1-\mu}{\rho_{13}^3}\eta - \frac{\mu}{\rho_{23}^3}\eta \tag{2.26b}$$

$$\ddot{z} = -\frac{1-\mu}{\rho_{13}^3}z - \frac{\mu}{\rho_{23}^3}z \tag{2.26c}$$

### 2.2.2 Jacobi's integral

Over the last centuries many efforts were made to solve analytically the CR3BP, as reported extensively in Szebehely's work [11]. One of the greatest achievements made in this field is the discover of an integral, named after Jacobi: this result is a pseudo-integral of motion in the synodic RF, pivotal to understand the regions that are accessible for a satellite in the binary system.

To derive such integral, a potential function $U$ in the inertial RF is defined

$$U_F = \frac{\mu_1}{r_{13}} + \frac{\mu_2}{r_{23}} \tag{2.27}$$

To switch to the synodic RF one has to take into consideration the centrifugal potential and Equation (2.27) becomes

$$U_R = \frac{\mu_1}{r_{13}} + \frac{\mu_2}{r_{23}} + \frac{1}{2}\omega_S(x^2 + y^2) \tag{2.28}$$

or, in non-dimensional form

$$\mathcal{U}_R = \frac{1-\mu}{\rho_{13}} + \frac{\mu}{\rho_{23}} + \frac{1}{2}(\xi^2 + \eta^2) \tag{2.29}$$

In the CR3BP domain, $\mathcal{U}$ is known as *pseudopotential.*

Then, one can derive the first order derivatives of such quantity with respect to the three non-dimensional position states

$$\frac{\partial \mathcal{U}}{\partial \xi} = \xi - \frac{1-\mu}{\rho_{13}^3}(\xi + \mu) - \frac{\mu}{\rho_{23}^3}[\xi - (1-\mu)] \tag{2.30a}$$

$$\frac{\partial \mathcal{U}}{\partial \eta} = \eta - \frac{1-\mu}{\rho_{13}^3}\eta - \frac{\mu}{\rho_{23}^3}\eta \tag{2.30b}$$

$$\frac{\partial \mathcal{U}}{\partial \zeta} = -\frac{1-\mu}{\rho_{13}^3}\zeta - \frac{\mu}{\rho_{23}^3}\zeta \tag{2.30c}$$

which can be combined with Equation (2.26) to obtain

$$\ddot{\xi} - 2\dot{\eta} = \frac{\partial \mathcal{U}}{\partial \xi} \tag{2.31a}$$

$$\ddot{\eta} + 2\dot{\xi} = \frac{\partial \mathcal{U}}{\partial \eta} \tag{2.31b}$$

$$\ddot{z} = \frac{\partial \mathcal{U}}{\partial \zeta} \tag{2.31c}$$

Furthermore, it is necessary to multiplicate each equation in (2.25) by $2\dot{x}$, $2\dot{y}$ and $2\dot{z}$, respectively. By summing all the three results, one obtains

$$2\ddot{x}\dot{x} + 2\ddot{y}\dot{y} + 2\ddot{z}\dot{z} - 2\omega_S^2(\dot{x}x + \dot{y}y) = 2\dot{x}\frac{\partial U}{\partial x} + 2\dot{y}\frac{\partial U}{\partial y} + 2\dot{z}\frac{\partial U}{\partial z} = 2\frac{\partial U}{\partial t} \tag{2.32}$$

Finally, the Jacobi integral is obtained by integrating Equation (2.32)

$$V^2 = 2U - J_C \tag{2.33}$$

where $V^2 = \dot{x}^2 + \dot{y}^2 + \dot{z}^2$ is the velocity squared in the inertial RF, U the pseudopotential and $J_C$ the so-called *Jacobi constant*. Equation (2.33) presents similarities with the *vis-viva* Equation (2.6) in the 2BP, where the sum of the kinetic $V^2/2$ and the potential $-\mu/r$ energies becomes the total specific mechanical one $\mathcal{E}$: here, the greater $J_C$ is, the less energy the SC has in the synodic RF [7, 12]. In a non-dimentional form, preferred for the scope of this thesis, Equation (2.33) becomes

$$\mathcal{V}^2 = 2\mathcal{U} - \mathcal{J}_C \tag{2.34}$$

where $\mathcal{V}^2 = \dot{\xi}^2 + \dot{\eta}^2 + \dot{\zeta}^2$ is the velocity in the synodic RF.

As a result, Jacobi's integral provides a relation between the states of motion, namely the position $\xi$, $\eta$, $\zeta$ and the velocity $\dot{\xi}$, $\dot{\eta}$, $\dot{\zeta}$ states. In section (2.2.4) is discussed how such result can be exploited to understand the regions of possible motion.

### 2.2.3 Lagrangian points

Another important result comes from the work of Lagrange: during his studies on the CR3BP he discovered analytically the *equilibrium points*, now called Lagrangian Points (LPs) in his honour. The work has been presented in his *Essai sur le Problème des Trois Corps* [13], published in 1772 while he was teaching in Berlin.

Following Lagrange's work, the gradient of the pseudopotential is set to zero, which implies that all velocities and accelerations are nullified:

$$\nabla\mathcal{U} = \mathbf{0} \tag{2.35}$$

Hence,

$$\frac{\partial\mathcal{U}}{\partial\xi} = 0 = \xi - \frac{1-\mu}{\rho_{13}^3}(\xi+\mu) - \frac{\mu}{\rho_{23}^3}[\xi-(1-\mu)] \tag{2.36a}$$

$$\frac{\partial\mathcal{U}}{\partial\eta} = 0 = \eta - \frac{1-\mu}{\rho_{13}^3}\eta - \frac{\mu}{\rho_{23}^3}\eta \tag{2.36b}$$

$$\frac{\partial\mathcal{U}}{\partial\zeta} = 0 = -\frac{1-\mu}{\rho_{13}^3}\zeta - \frac{\mu}{\rho_{23}^3}\zeta \tag{2.36c}$$

From Equations (2.36a) to (2.36c) one can find 5 set of coordinates $\{\xi_i\ \eta_i\ \zeta_i\}$, with $i = 1, ..., 5$, that can satisfy them.

In particular, Equation (2.36c) can be solved posing $\zeta = 0$, meaning that all the LPs are on the fundamental $\hat{\boldsymbol{\xi}}_S - \hat{\boldsymbol{\eta}}_S$ plane. The two remaining Equations can be solved via substitution: three roots are found setting $\eta = \zeta = 0$, called *collinear points*, while the other two, the *triangular points*, setting $\rho_{13} = \rho_{23} = 1$.

The three *collinear* points are the three LPs that lay on the $\hat{\boldsymbol{\xi}}_S$ axis, obtained from the following quintic

$$\xi^5 + (3-\mu)\xi^4 + (3-2\mu)\xi^3 - \mu\xi^2 - 2\mu\xi - \mu = 0 \tag{2.37}$$

while the other two form a triangle with the primaries, using their distance as base. In Figure (2.5) are shown the LPs of a generic system with $\mu = 0.1$, almost ten times larger than the one for Earth and Moon.

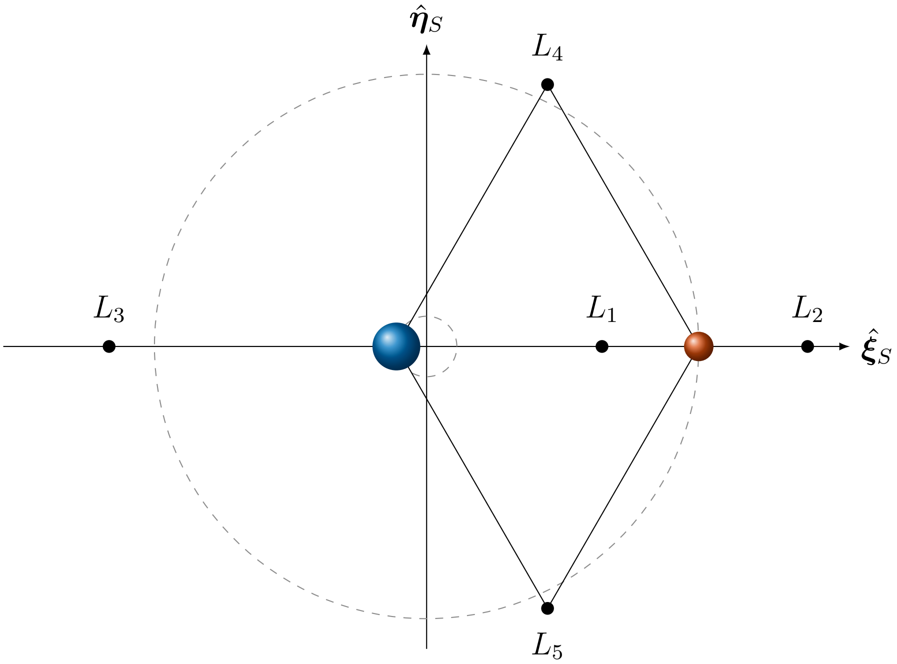

Figure 2.5: Lagrangian points of a generic binary system, $\mu = 0.1$

These points are also known as *singularity* or *equilibrium* points, as a SC is not subjected to any acceleration there (in the synodic RF). In fact, the equations of motion return

$$\begin{cases} \ddot{\xi} = 0 \\ \ddot{\eta} = 0 \\ \ddot{\zeta} = 0 \end{cases} \tag{2.38}$$

meaning that, without any perturbation, a still third body in such points does not move if seen in a synodic RF.

Over the last years, the LPs have been studied in depth and many missions were designed to leverage them. Of particular interest is the $L_2$ Earth-Sun point where, thanks to its dark and cold environment "behind" the Earth, extremely accurate observations can be made: NASA's James Webb Space Telescope [14] and ESA's Gaia [15] and Euclid [16] are prime examples.

A great in-depth analysis can be found in Szebehely's work [11], concerning the stability of the equilibrium points and the motions near them, but is beyond the scope of the present thesis.

### 2.2.4 Zero-velocity surfaces

By imposing a null velocity, relative to the synodic RF, in Equation (2.33), one can find

$$\mathcal{J}_C = 2\mathcal{U} \tag{2.39}$$

that provides a useful result to understand the regions of possible motion in the binary system. In fact, Equation (2.39) represents a surface, given a specific value for the constant $\mathcal{J}_C$, called *Zero-Velocity Surface*. These surfaces represent the spatial boundaries where the kinetic energy of a third body in the synodic frame nullifies, hence they delimit the energetically forbidden regions of motion.

If seen on the fundamental $\hat{\boldsymbol{\xi}}_S - \hat{\boldsymbol{\eta}}_S$ plane, the surfaces become curves: *Zero-Velocity Curves*.

A third body that is orbiting around a primary, with its velocity equal to the necessary orbital one, has a delimited region where it can move. If all its orbital energy is converted in altitude, it would reach the boundary of such region. If the SC increases its energy, using a thruster, for example, it would expand the region where it can move: the more it increases, the lower $\mathcal{J}_C$ becomes and the more space is accessible.

In Figure (2.6) is shown how the curves modify when the Jacobi constant decreases: it is very important for interplanetary transfers to ensure the right value in order to get to the celestial body and, if needed, to catch it.

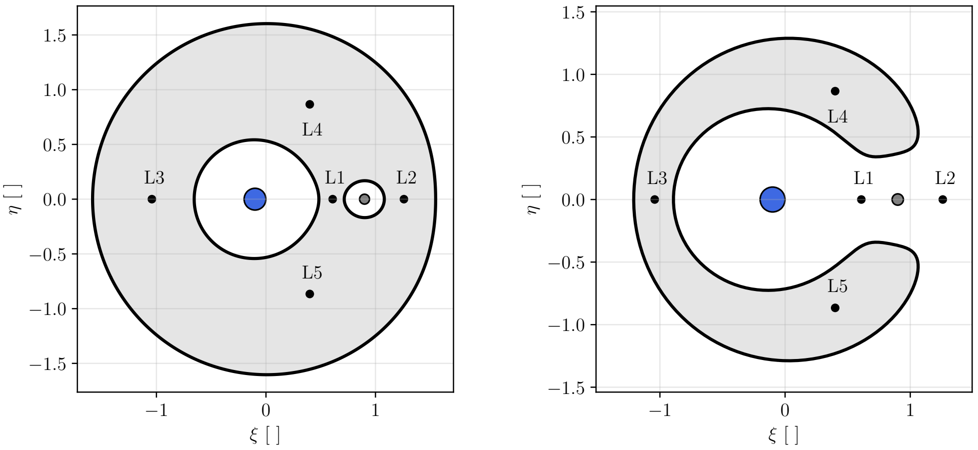

(a) $\mathcal{J}_C = 3.80$ (b) $\mathcal{J}_C = 3.18$

Figure 2.6: Zero-Velocity curves for different $\mathcal{J}_C$ with $\mu = 0.1$

## 2.3 Earth-Moon system

The focus of the present thesis is on trajectory optimisation in the Earth-Moon binary system. In the current Section the main characteristic of the system are discussed, referring to the Earth with the subscript $*_1$ or $*_{\text{♁}}$ and to the Moon with $*_2$ or $*_{\text{☾}}$ .

The adimensionalisation for a generic dynamical system can be performed in different ways, depending on the problem to be solved and its focus. For the scope of this thesis, the characteristic values are reported in Table (2.2): $l^*$ is the distance between the Earth and the Moon (constant, due to the hypothesis of the CR3BP), $m^*$ the sum of their masses and $\mathcal{T}^*$ is derived. As a result, the following pivotal non-dimensional quantities are obtained:

$$\begin{cases} \rho_{12} = 1 \\ \mu = 0.0121505843947097 \\ \tau = 2\pi \end{cases}$$

In this way, the non-dimensional time $\tau = 2\pi$ is equal to one complete rotation of the primaries around their barycentre, hence a period of 27.32166155 days, also known as *sidereal month.*

| | Value | Unit of Measurement |
|---|---|---|
| $l^*$ | $3.84400 \cdot 10^5$ | km |
| $m^*$ | $6.04542 \cdot 10^{24}$ | kg |
| $\mathcal{T}^*$ | $3.75196 \cdot 10^5$ | s |

Table 2.2: Characteristic values for the Earth-Moon system

As mentioned before, the only parameter of the system is the mass parameter $\mu$. Thanks to it, one can find the non-dimentional mass of the primaries, from Equation (2.12)

$$\mu_1 = 1 - \mu = 0.9878494156052903 \tag{2.40a}$$

$$\mu_2 = \mu = 0.0121505843947097 \tag{2.40b}$$

and, consequently, the position of the barycentre as per Equation (2.13)

$$\rho_{CG} = \mu = 0.0121505843947097 \tag{2.41}$$

that is located approximately 1700km below Earth's surface. As a result, the non-dimentional positions of the primaries with respect to the barycentre are

$$\rho_1 = -\mu = -0.0121505843947097 \tag{2.42a}$$

$$\rho_2 = 1 - \mu = 0.9878494156052903 \tag{2.42b}$$

In Table (2.3) is reported a summary of the Earth-Moon system values that are useful for the scope of this thesis, adding the non-dimentional mean radius of the two celestial bodies $P_{♁}$ and $P_{☾}$ [8, 17].

| Constant | Value [ ] |
|---|---|
| $\mu$ | 0.0121505843947097 |
| $\mu_1$ | 0.9878494156052903 |
| $\mu_2$ | 0.0121505843947097 |
| $\rho_1$ | $-0.0121505843947097$ |
| $\rho_2$ | 0.9878494156052903 |
| $\rho_{12}$ | 1.0000000000000000 |
| $P_{♁}$ | 0.0165920915712799 |
| $P_{☾}$ | 0.0045187304890738 |

Table 2.3: Summary of useful Earth-Moon binary system values.

Furthermore, following the procedure in section (2.2.3), the values of the Lagrangian point of the Earth-Moon system are obtained and reported in Table (2.4). In this particular case, $L_1$ takes the name of *cislunar point*, $L_2$ *translunar point*, while $L_4$ and $L_5$ are called the *trojan points*.

| Point | $\xi$ | $\eta$ | $\zeta$ | $\mathcal{J}_C$ |
|---|---|---|---|---|
| $L_1$ | 0.83691507 | 0.00000000 | 0.00000000 | 3.188341 |
| $L_2$ | 1.15568221 | 0.00000000 | 0.00000000 | 3.172161 |
| $L_3$ | $-1.00506265$ | 0.00000000 | 0.00000000 | 3.012147 |
| $L_4$ | 0.48784940 | 0.86602540 | 0.00000000 | 2.987997 |
| $L_5$ | 0.48784940 | $-0.86602540$ | 0.00000000 | 2.987997 |

Table 2.4: Earth-Moon Lagrangian points

In Figure (2.7) is represented the Earth-Moon binary system and its equilibrium points (radius not in scale).

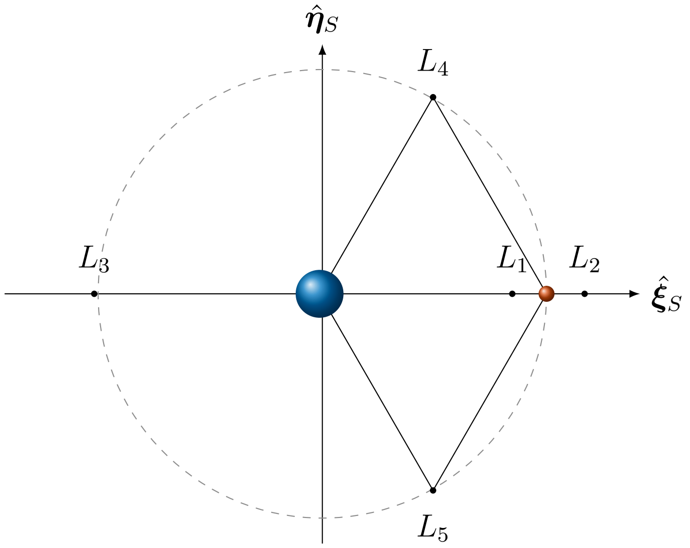

Figure 2.7: Earth-Moon system's Lagrangian points

## 2.4 Electric Propulsion

Electric Propulsion (EP) encompasses any propulsion technology in which electric power is used to increase the propellant exhaust velocity and generate thrust [18]. Achieving higher specific impulse than traditional chemical thrusters, the required amount of fuel for a determinate manoeuvre, or mission, is decreased, allowing for a reduction in total launch mass or an increase in scientific payload capacity.

Consequently, the past six decades have seen intense development in EP, making it suitable for various scenarios. Current applications are diverse, ranging from precise station-keeping and orbit insertion for telecommunication satellites to serving as the primary propulsion system for deep-space exploration.

Electric thrusters present a wide variety of different architectures, typically categorised by the physical mechanism used to accelerate the propellant: electrothermal, electrostatic and electromagnetic.

### 2.4.1 Performance

The fundamental principle of space propulsion relies on the conservation of momentum. In general, the thrust $T$ on a spacecraft is equal to the time rate of change of the propellant's momentum, which is the product of the exhaust velocity $c$ per the mass flow rate $\dot{m}_p$

$$T = \frac{d}{dt}(m_p \cdot c) = \dot{m}_p \cdot c \tag{2.43}$$

where $m_p$ is the propellant mass. To generate a specific thrust level, for space applications the best strategy to seek is to achieve the highest exhaust velocity possible to minimise the mass flow rate, thus preserving the propellant.

The primary objective of any propulsion system is to alter the spacecraft's state of motion. The resultant variation in velocity $\Delta V$ is given by the integral of the acceleration over the burn time $\Delta t$:

$$\Delta V = \int_0^{\Delta t} \frac{T}{m}\, dt \tag{2.44}$$

Integrating this expression provides the Tsiolkovsky equation, that establishes a correlation between the manoeuvre cost, the propellant mass $m_p = m_0 - m_f$, and the effect, $\Delta V$:

$$\Delta V = c \ln \frac{m_0}{m_f} \tag{2.45}$$

From Equation (2.45) the required propellant mass $m_p$ can be expressed as

$$m_p = m_0 - m_f = m_0 \left(1 - e^{-\Delta V / c}\right) \tag{2.46}$$

By introducing the specific impulse

$$I_{\mathrm{sp}} = \frac{c}{g_0} \tag{2.47}$$

where $g_0 = 9.8067$ m/s$^2$ is the gravitational acceleration, Tsiolkovsky's equation becomes

$$\Delta V = I_{\mathrm{sp}} \cdot g_0 \cdot \ln \frac{m_0}{m_f} \tag{2.48}$$

The fundamental result retrieved from Equation (2.46) highlights that, for a given mission with fixed $\Delta V$ and $m_0$, the required propellant can be reduced by increasing the exhaust velocity $c$ (thus the specific impulse $I_{\mathrm{sp}}$).

For conventional chemical thrusters, the exhaust velocity is limited by the energy contained in the chemical bounds of the propellant used [18]; even for high-energy bipropellants like liquid oxygen LOX and liquid hydrogen $c$ is constrained to $\approx$ 4km/s. On the other hand, electric propulsion decouples the propellant from the energy source, thus does not suffer from this limitation, assuming values up to 40 km/s. Considering the available electric power $P_E$ and its relative efficiency $\eta_E$, the energy balance on the propellant mass flow rate is

$$\eta_E P_E = \dot{m}_p \frac{c^2}{2} = \frac{T \cdot c}{2} \tag{2.49}$$

from which

$$c = \sqrt{\frac{2\eta_E P_E}{T}} \tag{2.50}$$

As a result, one can observe that $c$ can be increased by either increasing $P_E$ or decreasing $T$. Consequently, EP is characterised by low thrust, where the acceleration is just a fraction of $g_0$. While these systems cannot provide the high-thrust-to-weight ratios needed for planetary liftoff, their characteristics makes them suitable for high-$\Delta V$ missions.

### 2.4.2 Edelbaum transfer

A consequence of the low-thrust nature of EP is the extended duration of manoeuvres, resulting in a slow, continuous perturbation of the orbital trajectory. This scenario is opposite to high-thrust chemical systems, that apply large thrust over short time periods: thus, manoeuvres can be considered impulsive and the modification of the orbital state instantaneous.

Therefore, to analyse continuous low-thrust trajectories, alternative methods are required. One fundamental result was provided by T. N. Edelbaum, that exploited Gauss' Perturbation Equations adapting them to a low-thrust context.

For the scope of the present research, the focus is on the variation of the semi-major axis to determine the optimal thrust direction for orbital raising. Within the 2BP context and using a Velocity-Normal-Binormal (V-N-B) RF, the rate of change for $a$ is

$$\frac{da}{dt} = \frac{2a^2}{\sqrt{\mu a(1-e^2)}} \left[ e \sin\nu \; T_N + (1 + e\cos\nu) \; T_V \right] \tag{2.51}$$

where $a, e, \nu$ represent the orbital elements, $\mu$ is the gravitational parameter and $T_N$, $T_V$ the radial and tangential thrust components, respectively. For Edelbaum's approximation, three assumptions are now required:

- The orbital eccentricity remains small throughout the manoeuvre;
- The magnitude of acceleration on the SC is significantly lower than the gravitational acceleration $g_0$;

- The transfer time is long relative to the orbital period.

Under these three assumptions, Equation (2.51) becomes

$$\frac{da}{dt} = 2\sqrt{\frac{a^3}{\mu}}\frac{T_V}{m} \tag{2.52}$$

Assuming a constant acceleration magnitude ($a = T/m \approx$ const), it results helpful to express the thrust components in terms of two angles: $\alpha$, the angle between the velocity vector and the component of $T$ on the orbital plane, and $\beta$, the out-of-plane angle. Thus, $T_V = T \cos\alpha \cos\beta$, and, substituting it in Equation (2.52), yields

$$\frac{da}{dt} = 2\sqrt{\frac{a^3}{\mu}}\frac{T}{m}\cos\alpha\cos\beta \tag{2.53}$$

In this way, one can obtain the optimal angle to perform a desired manoeuvre, namely a variation of the semi-major axis in this case. To maximise the effect on $a$, the solution is

$$\begin{cases} \alpha & = 0, \pi \\ \beta & = 0 \end{cases} \tag{2.54}$$

thus, the optimal thrust direction is tangential to the orbit: $\alpha = 0$ corresponds to a raising manoeuvre, while $\alpha = \pi$ to a descent. The result of this continuous tangential acceleration is a characteristic spiral trajectory, illustrated in Figure (2.8). Further details on inclination and eccentricity variations can be found in [19].

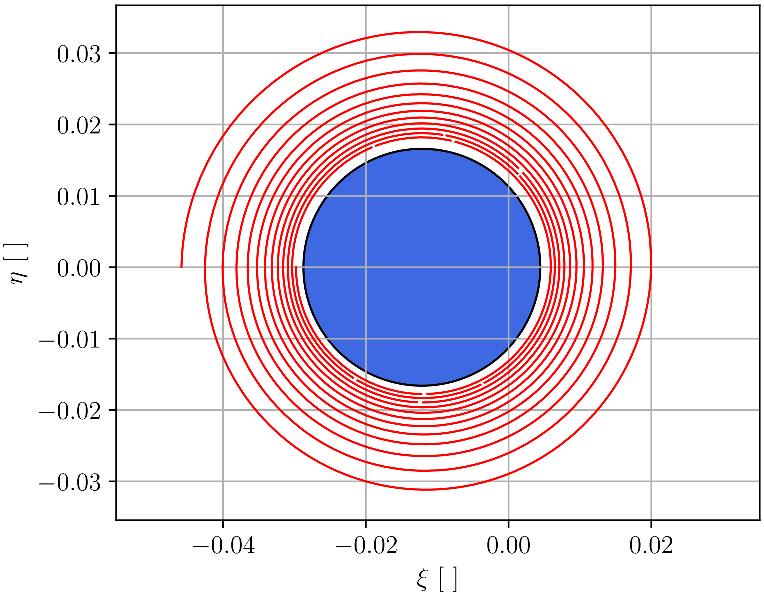

Figure 2.8: Example of a coplanar circle to circle transfer

# 3 | Optimal Control Theory

This Chapter treats the insight of the Optimal Control Theory. An overview of direct and indirect methods is offered, then it is shown how the Optimal Control Problem is defined and solved: Two Points Boundary Value Problem (TPBVP) and Multi-Point Boundary Value Problem (MPBVP) are here introduced. In the end, in section (3.5) the Optimal Control Problem of interest for the current thesis is presented.

The structure and contents are based on the work of Mascolo [12].

## 3.1 Optimal Control Problem

In the current Space environment, low-thrust trajectories are required for certain missions and their optimisation is a fundamental aspect.

An Optimal Control Problem (OCP) researches the control law that maximises or minimises a merit index. In particular, the optimal trajectory is the one that minimises fuel usage (or maximum final mass) during the transfer, since in space propellant is a limited resources that impacts heavily on the mission.

To do so, specific parameters shall be controlled all over the trajectory to find the control variables that maximise the performance index, such as thrust duration and direction.

### 3.1.1 Direct versus Indirect Numerical Methods

A numerical method is an algorithm with theoretical properties, the purpose of which is to find an approximate solution to a mathematical model. Generally, it decomposes the problem into smaller and simpler ones: the *transcription* procedure converts a infinite-dimensional problem into a finite-dimensional one. The considered trajectory optimisation problem is continuous and such procedure has to be applied in order to obtain a problem with a finite set of variables.

Numerical methods are classified into direct and indirect. Each group can be employed to solve OCPs and present different characteristics: a in-depth view is provided by Betts [20].

For a generic OCP direct methods are preferred, thanks to their prompt implementation. They try to find directly a minimum of the merit function $F$ constructing a sequence of points where $F$ decreases: this is called the *mesh* and discretises the state and the optimal controls. In such way a direct method results robust and able to handle complex problems. However, to obtain accurate results, the mesh has to be very dense, meaning that it requires a large number of nodes, impacting heavily on the computational cost. In some cases refining techniques for the mesh are required. These methods are implemented, for example, in commercial software such as GMAT by NASA [21] and STK by Ansys [22].

On the other hand, Indirect Methods (IMs) work on the derivative of the merit function and attempt to locate the root of the necessary conditions. To do so, one has to explicit the adjoint equations, control equations and transversality conditions: the problem may appear more complicated, but IMs provide theoretical tools that help the user to find the optimal solution. Solutions are more accurate and usually require minimal computational cost, however they are very sensitive to initial conditions, requiring a good guess to converge. IMs are employed in many software (e.g. NASA's SEPSPOT) and research groups, like at Politecnico di Torino [12, 20, 23].

## 3.2 Optimal control theory

As mentioned before, the aim of a Optimal Control Theory applied to OCPs is to compute the control law that takes the performance index to the extreme.

The dynamics of a OCP is defined by a set of first-order ODEs that, in explicit form is

$$\dot{\boldsymbol{x}} = \boldsymbol{f}(\boldsymbol{x}(t), \boldsymbol{u}(t), t) \tag{3.1}$$

Equation (3.1) describes the evolution of the state vector $\boldsymbol{x} \in \mathbb{R}^n$ between initial and final time (as $t$ is the independent variable). This evolution depends on the state itself, as well as the control vector $\boldsymbol{u} \in \mathbb{R}^m$ and time $t$. An optimal solution is the one that provides $\boldsymbol{x}^*(t)$, under the optimal control $\boldsymbol{u}^*(t)$, maximising the performance index.

In a general case, a trajectory can be treated as a TPBVP. Its extremal points at initial and final time $(t_0, t_f)$ are subject to boundary conditions called *extremal conditions*, later mentioned as initial conditions and target.

All the Boundary Conditions (BCs) are collected in the constraint vector

$$\boldsymbol{\chi}(\boldsymbol{x_0}, \boldsymbol{x_f}, t_0, t_f) = \mathbf{0} \tag{3.2}$$

where $\boldsymbol{\chi} : [\mathbb{R}^n, \mathbb{R}^n, \mathbb{R}, \mathbb{R}] \rightarrow \mathbb{R}^q$.

Also the control vector $\boldsymbol{u}(t)$ can be constrained, allowing it to assume a limited set of values.

It is clear now that one of the most important features is the merit index, that can be expressed as

$$\mathcal{J} = \varphi(\boldsymbol{x}_0, \boldsymbol{x}_f, t_0, t_f) + \int_{t_0}^{t_f} [\Phi(\boldsymbol{x}(t), \boldsymbol{u}(t), t)]\, dt \tag{3.3}$$

and presents two scalar terms. The function $\varphi$ depends on the state and the time at the extremal points, neglecting how the solution evolves; on the other hand, the integral of the function $\Phi$ takes into account the values of state and control inputs over time, as well as time itself.

Equation (3.3), as written, is known as *Bolza's problem*: the aim is to optimise a set of ODEs between an initial and final time, under specific BCs. Alternative forms of the merit index are available, when desired: Lagrange's formulation imposes $\phi = 0$, while Mayer's nullifies $\Phi$.

To proceed with Indirect Methods and to access their theoretical insights, is now necessary a manipulation of the merit index. The optimality conditions provided by IMs are found introducing an augmented merit function $\mathcal{J}^*$, that measures how much state and BCs are respected. This is possible with the introduction of adjoint variables, associated with state ones, and the Lagrange multipliers, linked to the BCs. They are grouped, respectively, in the following vectors

$$\boldsymbol{\lambda}(t) \in \mathbb{R}^n \tag{3.4}$$

$$\boldsymbol{\mu} \in \mathbb{R}^q \tag{3.5}$$

Therefore, the augmented merit function can be expressed as

$$\mathcal{J}^* = \varphi + \boldsymbol{\mu}^T \boldsymbol{\chi} \int_{t_0}^{t_f} [\Phi + \boldsymbol{\lambda}^T (\boldsymbol{f} - \dot{\boldsymbol{x}})]\, dt \tag{3.6}$$

where, for the sake of brevity,

$$\varphi = \varphi(\boldsymbol{x}_0, \boldsymbol{x}_f, t_0, t_f) \tag{3.7a}$$

$$\Phi = \Phi(\boldsymbol{x}(t), \boldsymbol{u}(t), t) \tag{3.7b}$$

$$\boldsymbol{\chi} = \boldsymbol{\chi}(\boldsymbol{x_0}, \boldsymbol{x_f}, t_0, t_f) \tag{3.7c}$$

In the case that both BCs and state quantities are respected during the evolution of the dynamical model, then it appears that

$$\boldsymbol{\chi} = \mathbf{0} \tag{3.8a}$$

$$\dot{\boldsymbol{x}} = \boldsymbol{f} \tag{3.8b}$$

As a result, one can state that $\mathcal{J} = \mathcal{J}^*$; in any other case Equations (3.8a) and (3.8b) are violated and the statement results false.

It follows that, if all the constrains are respected, one can solve a OCP with the merit function expressed with either Equation (3.3) or (3.6), as they are mathematically equivalent.

Since the time derivatives of the state vector $\boldsymbol{x}$ are generally unknown during the optimisation, it results useful to eliminate them from the merit index, integrating the term $\boldsymbol{\lambda}^T \dot{\boldsymbol{x}}$ in Equation (3.6) by part:

$$\int_{t_0}^{t_f} -\boldsymbol{\lambda}^T \dot{\boldsymbol{x}}\, dt = -\left(\boldsymbol{\lambda}_f^T \dot{\boldsymbol{x}}_f\right) + \left(\boldsymbol{\lambda}_0^T \dot{\boldsymbol{x}}_0\right) + \int_{t_0}^{t_f} \left(\dot{\boldsymbol{\lambda}}^T \boldsymbol{x}\right)\, dt \tag{3.9}$$

By substituting Equation (3.9) into Equation (3.6), one can find

$$\mathcal{J}^* = \varphi + \boldsymbol{\mu}^T \boldsymbol{\chi} + \left(\boldsymbol{\lambda}_0^T \dot{\boldsymbol{x}}_0 - \boldsymbol{\lambda}_f^T \dot{\boldsymbol{x}}_f\right) + \int_{t_0}^{t_f} \left(\Phi + \boldsymbol{\lambda}^T \boldsymbol{f} - \dot{\boldsymbol{\lambda}}^T \boldsymbol{x}\right)\, dt \tag{3.10}$$

In Equation (3.10) appears a useful quantity, the system's Hamiltonian $\mathcal{H}$

$$\mathcal{H} \triangleq \Phi + \boldsymbol{\lambda}^T \boldsymbol{f} \tag{3.11}$$

To find the maximum (or the minimum) of the merit index $\mathcal{J}^*$ respecting the optimality conditions, implies that $\mathcal{J}^*$ has to be a stationary point, thus his first order variation must be null. The first order differentiation $\delta\mathcal{J}^*$ is here obtained

$$\begin{aligned}
\delta\mathcal{J}^* = &\left(\frac{\partial\varphi}{\partial t_0} + \boldsymbol{\mu}^T\frac{\partial\boldsymbol{\chi}}{\partial t_0} - \mathcal{H}_0\right)\delta t_0 + &\text{(3.12a)}\\
&+\left(\frac{\partial\varphi}{\partial t_f} + \boldsymbol{\mu}^T\frac{\partial\boldsymbol{\chi}}{\partial t_f} - \mathcal{H}_f\right)\delta t_f + &\text{(3.12b)}\\
&+\left(\frac{\partial\varphi}{\partial \boldsymbol{x}_0} + \boldsymbol{\mu}^T\frac{\partial\boldsymbol{\chi}}{\partial \boldsymbol{x}_0} - \boldsymbol{\lambda}_0^T\right)\delta \boldsymbol{x}_0 + &\text{(3.12c)}\\
&+\left(\frac{\partial\varphi}{\partial \boldsymbol{x}_f} + \boldsymbol{\mu}^T\frac{\partial\boldsymbol{\chi}}{\partial \boldsymbol{x}_f} - \boldsymbol{\lambda}_f^T\right)\delta \boldsymbol{x}_f + &\text{(3.12d)}\\
&+\int_{t_0}^{t_f}\left[\left(\frac{\partial\mathcal{H}}{\partial\boldsymbol{x}} + \dot{\boldsymbol{\lambda}}^T\right)\delta\boldsymbol{x} + \frac{\partial\mathcal{H}}{\partial\boldsymbol{u}}\delta\boldsymbol{u}\right]dt &\text{(3.12e)}
\end{aligned}$$

A specific set of adjoint variables $\boldsymbol{\lambda}$ and Lagrange's multipliers $\boldsymbol{\mu}$ can nullify Equation (3.12) for any choice of $\delta t_0$, $\delta t_f$, $\delta\boldsymbol{x}_0$, $\delta\boldsymbol{x}_f$ and $\delta\boldsymbol{u}$ by nullifying their coefficient.

From Equation (3.12) can be derived different sets of condition, one of each descending from a specific term of the Equation: lines (3.12a) and (3.12b) provide two transversality conditions at initial and final time when their coefficient is null; $2n$ optimality conditions are obtained from lines (3.12c) and (3.12d); finally, the last two coefficients provide $n$ Euler-Lagrange ODEs for the adjoint variables and $m$ algebraic equations for the control.

### 3.2.1 Boundary conditions for optimality

The boundary conditions for optimality set the behave of time and state at the extremal points of the trajectory, via 2 transversality and $2n$ optimality conditions, respectively. These conditions can be found by nullifying the coefficient of the first four lines in Equation (3.12):

$$\begin{aligned}
&\frac{\partial\varphi}{\partial t_0} + \boldsymbol{\mu}^T\frac{\partial\boldsymbol{\chi}}{\partial t_0} - \mathcal{H}_0 = 0 &\text{(3.13a)}\\
&\frac{\partial\varphi}{\partial t_f} + \boldsymbol{\mu}^T\frac{\partial\boldsymbol{\chi}}{\partial t_f} - \mathcal{H}_f = 0 &\text{(3.13b)}\\
&\frac{\partial\varphi}{\partial \boldsymbol{x}_0} + \boldsymbol{\mu}^T\frac{\partial\boldsymbol{\chi}}{\partial \boldsymbol{x}_0} - \boldsymbol{\lambda}_0^T = \boldsymbol{0} &\text{(3.13c)}\\
&\frac{\partial\varphi}{\partial \boldsymbol{x}_f} + \boldsymbol{\mu}^T\frac{\partial\boldsymbol{\chi}}{\partial \boldsymbol{x}_f} - \boldsymbol{\lambda}_f^T = \boldsymbol{0} &\text{(3.13d)}
\end{aligned}$$

From the transversality Equations (3.13a) and (3.13b), one can find that if the time is unconstrained and it does not appear in the scalar function $\varphi$, then the Hamiltonian is null at both initial and final time, while their values are subject to optimisation. On the other hand, if time is constrained (e.g. $t_0 = a$ and $t_f = b$), the Hamiltonian is free and its value depends on the optimisation.

A similar correlation can be found in optimality Equations (3.13c) and (3.13d), where if a state $x_i$ is unconstrained and does not appear in $\varphi$, then its associated costate $\lambda_{x_i}$ is null at the same point. The opposite case happens when the state is constrained.

A schematic flowchart for transversality and optimality conditions, from Mascolo's work [12], is shown in Figure (3.1).

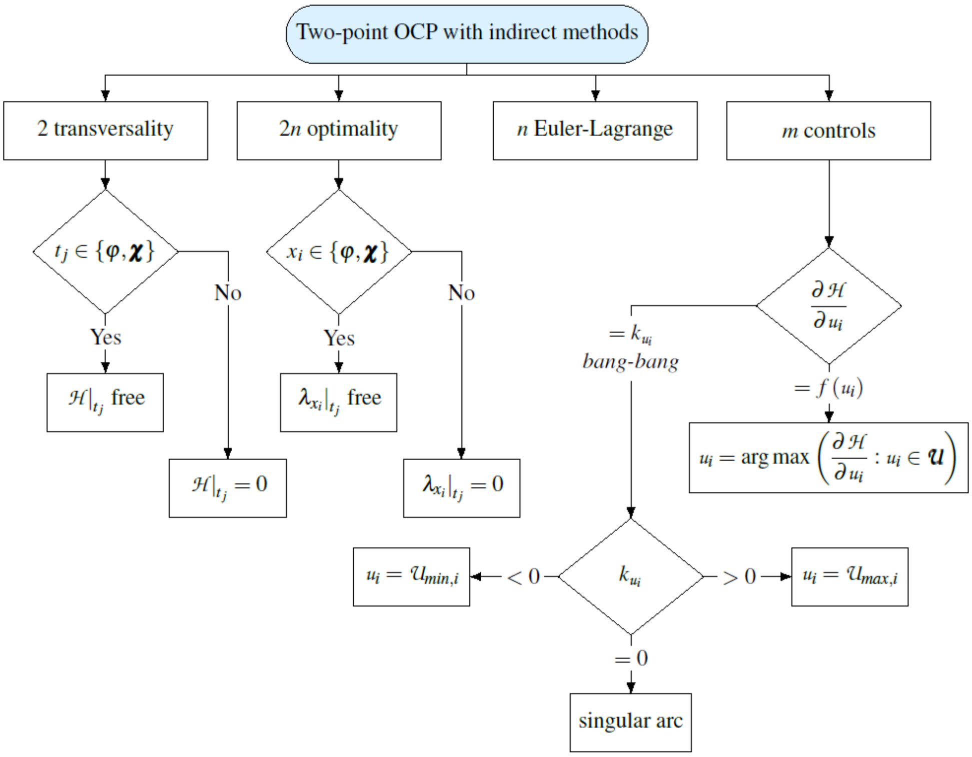

Figure 3.1: Rules for transversality and optimality conditions [12]

### 3.2.2 Equations for adjoint and control variables

From Equation (3.12d), one can find the set of ODEs that describe the evolution of the adjoint variables and controls over time. In particular, by nullifying the coefficient of $\delta \boldsymbol{x}$, Euler-Lagrange equations for the adjoint variables are obtained

$$\frac{d\boldsymbol{\lambda}}{dt} = -\left(\frac{\partial \mathcal{H}}{\partial \boldsymbol{x}}\right)^T \tag{3.14}$$

On the other hand, when it is the coefficient of $\delta\boldsymbol{u}$ being nullified, $m$ algebraic control equations are found

$$\left(\frac{\partial \mathcal{H}}{\partial \boldsymbol{u}}\right)^T = 0 \tag{3.15}$$

In the most general case, the control vector $\boldsymbol{u}$ or a part of its components may be bounded to a specific limit, say $\mathcal{U}$: in the present thesis only explicit boundaries are considered, for example by limiting $\boldsymbol{u}$ between two extremes $\mathcal{U}_{\min} \leq u \leq \mathcal{U}_{\max}$. It is noted that generally the controls depend on the state variables and time, as $\boldsymbol{u}(\boldsymbol{x}(t), t)$.

Under the constraint of explicit boundaries, the optimal control vector $\boldsymbol{u}^* \in \mathcal{U}$ is the one that, per each point in the desired trajectory, extremizes the Hamiltonian in Equation (3.11) in that specific point. This fundamental result is defined as Pontryagin's Maximum Principle (PMP).

However, if the Hamiltonian in Equation (3.11) is linear with respect to the control, Equation (3.15) cannot hold. Thus

$$\frac{\partial \mathcal{H}}{\partial u_i} = \begin{cases} k_{u_i} & \text{if } \mathcal{H} \text{ is linear wrt } u_i \\ f(u_i) & \text{otherwise} \end{cases} \tag{3.16}$$

where $k_{u_i}$ is a constant. If the Hamiltonian is linear with respect to the control, Equation (3.16) cannot be fulfilled, as $u_i$ cannot appear explicitly. Under these conditions, one has to seek the strategy dependent on the provided constant $k_{u_i}$. In particular, considering $k_{u_i} \neq 0$, to respect the PMP $\mathcal{H}$ is maximised imposing the maximum admissible value for the control, $u_i = \mathcal{U}_{i,\max}$ for $k_{u_i} > 0$ or the minimum, $u_i = \mathcal{U}_{i,\min}$ for $k_{u_i} < 0$. Such result is defined as *bang-bang* control and it is implemented in the present thesis: $\mathcal{H}$ is linear with respect to the thrust $T$, the unique control variable that switches between a maximum value $T_{\max}$ and a minimum $T_{\min}$, assumed null.

The Euler-Lagrange and control equations complete the flowchart in Figure (3.1).

As a result, in the TPBVP here presented, one obtains $2+2n+m$ equations: transversality (3.13a, 3.13b), optimality (3.13c, 3.13d) and control (3.15).

## 3.3 Multi-Point Optimal Control Problem

When the boundary conditions are imposed also in internal points of the trajectory, the problem becomes a MPBVP. The trajectory may be divided into $n_p$ subintervals, called *arcs*, created to improve the robustness of the code and to aid the convergence. Variables are continuous along each arch, but may present discontinuities at the internal boundaries, those points where the conditions are imposed and that link two adjacent arcs. In this way, Equations (3.1) to (3.3) define a MPBVP. Each j-th arc starts at a $t_{(j-1)+}$ and ends at $t_{j-}$, while the extremal state vector are, respectively, $\boldsymbol{x}_{(j-1)+}$ and $\boldsymbol{x}_{j-}$; every arc spans over a generic duration $\delta t_j$, subject to optimisation.

In Figure (3.2) is illustrated the schema of the generic MPBVP, considering $\boldsymbol{x}(t_j) \triangleq \boldsymbol{x}_j$ for the sake of brevity.

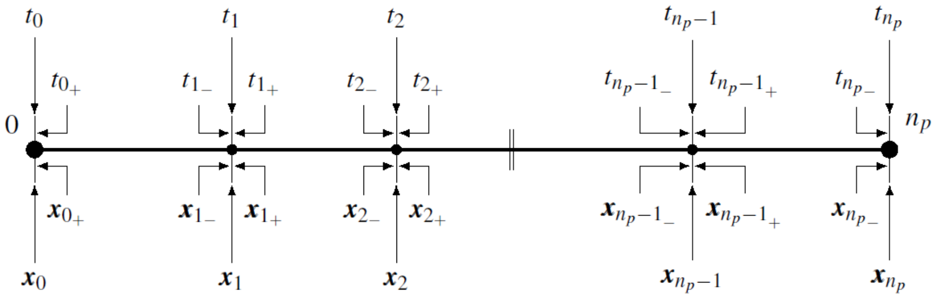

Figure 3.2: Schema of the generic MPBVP [12]

As mentioned before, in the MPBVP the boundary conditions can be imposed in the internal points and are added to the extremal ones in Equation (3.2). Those new BCs can be expressed as

$$\boldsymbol{\chi}(\boldsymbol{x}_{(j-1)_+}, \boldsymbol{x}_{j_-}, t_{(j-1)_+}, t_{j_-}) = \boldsymbol{0}, \qquad j = 1, \ldots, n_p \tag{3.17}$$

and may depend on both the state and the time variable.
Therefore, the merit index for the MPBVP is

$$\mathcal{J} = \varphi(\boldsymbol{x}_{(j-1)_+}, \boldsymbol{x}_{j_-}, t_{(j-1)_+}, t_{j_-}) + \sum_{j=1}^{n_p} \int_{t_{(j-1)_+}}^{t_{j_-}} [\Phi(\boldsymbol{x}(t), \boldsymbol{u}(t), t)]\, dt \tag{3.18}$$

and here $\varphi$ depends on the value the state variables assume at every boundary, both for the complete trajectory, from $j = 0$ to $j = n_p$, and for each arc. For what concerns $\Phi$, it still depends on the evolution of state and control over time, but now considers how the solution evolves arc-by-arc.

Then, the augmented merit index for the MPBVP takes the form of

$$\mathcal{J}^* = \varphi + \boldsymbol{\mu}^T \boldsymbol{\chi} + \sum_{j=1}^{n_p} \int_{t_{(j-1)_+}}^{t_{j_-}} [\Phi + \boldsymbol{\lambda}^T (\boldsymbol{f} - \dot{\boldsymbol{x}})]\, dt \tag{3.19}$$

and, integrating by parts,

$$\mathcal{J}^* = \varphi + \boldsymbol{\mu}^T \boldsymbol{\chi} + \sum_{j=1}^{n_p} \left( \boldsymbol{\lambda}^T_{(j-1)_+} \dot{\boldsymbol{x}}_{(j-1)_+} - \boldsymbol{\lambda}^T_{j_-} \dot{\boldsymbol{x}}_{j_-} \right) + \sum_{j=1}^{n_p} \int_{t_{(j-1)_+}}^{t_{j_-}} \left( \Phi + \boldsymbol{\lambda}^T \boldsymbol{f} - \dot{\boldsymbol{\lambda}}^T \boldsymbol{x} \right) dt \tag{3.20}$$

The first order differentiation $\delta\mathcal{J}^*$, expressed for each arc, now becomes

$$\delta\mathcal{J}^* = \left( \frac{\partial \varphi}{\partial t_{(j-1)_+}} + \boldsymbol{\mu}^T \frac{\partial \boldsymbol{\chi}}{\partial t_{(j-1)_+}} - \mathcal{H}_{(j-1)_+} \right) \delta t_{(j-1)_+} + \tag{3.21a}$$

$$+ \left( \frac{\partial \varphi}{\partial t_{j_-}} + \boldsymbol{\mu}^T \frac{\partial \boldsymbol{\chi}}{\partial t_{j_-}} - \mathcal{H}_{j_-} \right) \delta t_{j_-} + \tag{3.21b}$$

$$+ \left( \frac{\partial \varphi}{\partial \boldsymbol{x}_{(j-1)_+}} + \boldsymbol{\mu}^T \frac{\partial \boldsymbol{\chi}}{\partial \boldsymbol{x}_{(j-1)_+}} - \boldsymbol{\lambda}^T_{(j-1)_+} \right) \delta \boldsymbol{x}_{(j-1)_+} + \tag{3.21c}$$

$$+ \left( \frac{\partial \varphi}{\partial \boldsymbol{x}_{j_-}} + \boldsymbol{\mu}^T \frac{\partial \boldsymbol{\chi}}{\partial \boldsymbol{x}_{j_-}} - \boldsymbol{\lambda}^T_{j_-} \right) \delta \boldsymbol{x}_{j_-} + \tag{3.21d}$$

$$+ \sum_{j=1}^{n_p} \int_{t_{(j-1)_+}}^{t_{j_-}} \left[ \left( \frac{\partial \mathcal{H}}{\partial \boldsymbol{x}} + \dot{\boldsymbol{\lambda}}^T \right) \delta \boldsymbol{x} + \frac{\partial \mathcal{H}}{\partial \boldsymbol{u}} \delta \boldsymbol{u} \right] dt, \qquad j = 1, \ldots, n_p \tag{3.21e}$$

In the MPBVP domain, it is more convenient to express the transversality and optimality conditions in terms of the j-th boundary itself. Therefore, the values immediately before and after the boundary are written as

$$\frac{\partial \varphi}{\partial t_{j_+}} + \boldsymbol{\mu}^T \frac{\partial \boldsymbol{\chi}}{\partial t_{j_+}} - \mathcal{H}_{j_+} = 0, \qquad j = 1, \ldots, n_p - 1 \tag{3.22a}$$

$$\frac{\partial \varphi}{\partial t_{j_-}} + \boldsymbol{\mu}^T \frac{\partial \boldsymbol{\chi}}{\partial t_{j_-}} - \mathcal{H}_{j_-} = 0, \qquad j = 1, \ldots, n_p \tag{3.22b}$$

$$\frac{\partial \varphi}{\partial \boldsymbol{x}_{j_+}} + \boldsymbol{\mu}^T \frac{\partial \boldsymbol{\chi}}{\partial \boldsymbol{x}_{j_+}} - \boldsymbol{\lambda}^T_{j_+} = \boldsymbol{0}, \qquad j = 1, \ldots, n_p - 1 \tag{3.22c}$$

$$\frac{\partial \varphi}{\partial \boldsymbol{x}_{j_-}} + \boldsymbol{\mu}^T \frac{\partial \boldsymbol{\chi}}{\partial \boldsymbol{x}_{j_-}} - \boldsymbol{\lambda}^T_{j_-} = \boldsymbol{0}, \qquad j = 1, \ldots, n_p \tag{3.22d}$$

Moreover, in such domain, the considerations on Euler-Lagrange equations for adjoint variables and control equations remain unchanged.

## 3.4 Implementation of the Boundary Value Problem

The scope of the present thesis is to perform Earth-Moon transfers trajectory optimisation in a medium-fidelity model, using low-thrust electric propulsion.

Simple strategies, such as single-shooting methods, are here implemented to improve the initial guess and solve the problem.

### 3.4.1 Single-shooting method

One of the simplest methods to find a specified path from an initial state $\boldsymbol{X}(t_0)$ to a desired final state $\boldsymbol{X}(\boldsymbol{X}(t_0), t_f)$ is to select an initial guess for the initial state and integrate it for a specified duration. If the final state is not close enough to the desired one, a correction is made, randomly or discretely, until they match: such method is based on trial-and-error, but does not have any information that the correction actually helps the convergence.

Another strategy that can be adopted is to understand how the initial state should be corrected in order to obtain the desired final one: this method proves to be more robust and provides theoretical insight of the evolution of the error over the iterations. This scenario is the classic framework for a TPBVP.

In summary, the aim of the "shooting" procedure is to correct an initial state until a set of final conditions are respected. This recursive method computes corrections for undesired terminal errors and updates the initial state at every *r-th* step to reduce them. However, not every state in $\boldsymbol{X}(t_0)$ may be allowed to change, while some final conditions may assume any value. Therefore, the free-variable vector $\boldsymbol{X}(t_0) \in \mathbb{R}^n$ is

$$\boldsymbol{X}_0 \triangleq \boldsymbol{X}(t_0) = \{X_1, X_2, \dots, X_n\}^T \tag{3.23}$$

and may contain state variables such as position and velocity, but also integration times. On the other hand, the constraint vector targets the desired values. For example, in this thesis its focus is on the conditions to orbit around the Moon and its form may be

$$\boldsymbol{\chi}(\boldsymbol{X}_f) = \{\chi_1, \chi_2, \dots, \chi_m\} = \begin{Bmatrix} \xi - \xi^* \\ \eta - \eta^* \\ \zeta - \zeta^* \\ \dot{\xi} - \dot{\xi}^* \\ \dot{\eta} - \dot{\eta}^* \\ \dot{\zeta} - \dot{\zeta}^* \end{Bmatrix} \tag{3.24}$$

where $\boldsymbol{\chi}(\boldsymbol{X}_f) \in \mathbb{R}^m$.

Thus, the aim of the method shifts to the search of a specific initial state $\boldsymbol{X}_0^*$ that enables to get $\boldsymbol{\chi}(\boldsymbol{X}_f^*) = \boldsymbol{0}$. As mentioned before, it is useful to know *how* vary the free-variables vector: for this purpose, a first order Taylor expansion is required. In this way one can track the change of the constraint vector following an update of the initial state. Considering $\boldsymbol{X}$ the final state vector for a generic time $t > t_0$,

$$\boldsymbol{\chi}(\boldsymbol{X}) = \boldsymbol{\chi}(\boldsymbol{X}_0) + \frac{\partial \boldsymbol{\chi}(\boldsymbol{X}_0)}{\partial \boldsymbol{X}}(\boldsymbol{X} - \boldsymbol{X}_0) \tag{3.25}$$

The first order derivatives of the constraint vector with respect to the free-variable vector $\boldsymbol{X}$ form a Jacobian matrix $\boldsymbol{J}(\boldsymbol{\chi}(\boldsymbol{X}_0), \boldsymbol{X}) \in \mathbb{R}^{m \times n}$

$$\frac{\partial \boldsymbol{\chi}(\boldsymbol{X}_0)}{\partial \boldsymbol{X}} = \boldsymbol{J}(\boldsymbol{\chi}(\boldsymbol{X}_0), \boldsymbol{X}) = \begin{bmatrix} \frac{\partial \chi_1}{\partial X_1} & \frac{\partial \chi_1}{\partial X_2} & \cdots & \frac{\partial \chi_1}{\partial X_n} \\ \frac{\partial \chi_2}{\partial X_1} & \frac{\partial \chi_2}{\partial X_2} & \cdots & \frac{\partial \chi_2}{\partial X_n} \\ \vdots & \vdots & \ddots & \vdots \\ \frac{\partial \chi_m}{\partial X_1} & \frac{\partial \chi_m}{\partial X_2} & \cdots & \frac{\partial \chi_m}{\partial X_n} \end{bmatrix} \tag{3.26}$$

Taking into consideration the iterative nature of the method, the Taylor expansion can be rewritten as

$$\boldsymbol{\chi}(\boldsymbol{X}_{r+1}) = \boldsymbol{\chi}(\boldsymbol{X}_r) + \frac{\partial \boldsymbol{\chi}(\boldsymbol{X}_r)}{\partial \boldsymbol{X}_{r+1}}(\boldsymbol{X}_{r+1} - \boldsymbol{X}_r) \tag{3.27}$$

where the step $r + 1$ depends on the previous one, $r$.

Some shortenings are now introduced, to thin the notation

$$\boldsymbol{\chi}_r \triangleq \boldsymbol{\chi}(\boldsymbol{X}_r) \tag{3.28a}$$

$$\boldsymbol{J}(\boldsymbol{\chi}_r) \triangleq \boldsymbol{J}(\boldsymbol{\chi}(\boldsymbol{X}_r), \boldsymbol{X}_{r+1}) \tag{3.28b}$$

If a solution exists, then $\chi_{r+1} = \boldsymbol{0}$ and a generic iterative solution can be expressed as

$$\boldsymbol{\chi}_r + [\boldsymbol{J}(\chi_r)]\,(\boldsymbol{X}_{r+1} - \boldsymbol{X}_r) = \boldsymbol{0} \tag{3.29}$$

Therefore, at each iteration one can compute the free-variables vector $\boldsymbol{X}_r$ and the updated constraint vector $\boldsymbol{\chi}_r$ directly from the EoMs from $\boldsymbol{X}_r$:

$$\boldsymbol{X}_{r+1} = \boldsymbol{X}_r - [\boldsymbol{J}(\chi_r)]^{-1}\,\boldsymbol{\chi}_r \tag{3.30}$$

In the case that $n > m$, there are more variables than constraint and the minimum norm update is employed instead of Equation (3.30): it guides the solution to be as close as possible to $\boldsymbol{\chi}_r$, among the possible ones. This particular update takes the form of

$$\boldsymbol{X}_{r+1} = \boldsymbol{X}_r - [\boldsymbol{J}(\chi_r)]^T \left[\boldsymbol{J}(\chi_r)\boldsymbol{J}(\chi_r)^T\right]^{-1} \boldsymbol{\chi}_r \tag{3.31}$$

To allow smaller corrections for each iteration and aid the convergence, a relaxation parameter $\kappa_R$ is introduced; the modified iterative update processes result

$$\boldsymbol{X}_{r+1} = \boldsymbol{X}_r - \kappa_R [\boldsymbol{J}(\chi_r)]^{-1} \boldsymbol{\chi}_r \qquad \text{if} \quad n = m \tag{3.32a}$$

$$\boldsymbol{X}_{r+1} = \boldsymbol{X}_r - \kappa_R [\boldsymbol{J}(\chi_r)]^T \left[\boldsymbol{J}(\chi_r)\boldsymbol{J}(\chi_r)^T\right]^{-1} \boldsymbol{\chi}_r \qquad \text{if} \quad n > m \tag{3.32b}$$

This procedure is described in the most general way, meaning that one can adopt dimentional or non-dimentional quantities for the calculation; in the current thesis non-dimentional states are preferred.

### 3.4.2 Boundary Value Problem

The OCP converts the original Boundary Value Problem (BVP) into an augmented one, where some of the initial state variables may be unknown. Therefore, a new initial state vector $\boldsymbol{y}_0$ is defined, as a concatenation of state and adjoint variables

$$\boldsymbol{y}_0 = \begin{Bmatrix} \boldsymbol{x}_0^T \\ \boldsymbol{\lambda}_0^T \end{Bmatrix} \tag{3.33}$$

The aim of such BVP is to find an initial state $\boldsymbol{y}_0^*$ that allows to reach the final target $\boldsymbol{y}_f^*$ while fulfilling every BC, both the imposed and optimality ones. The method chosen to solve the problem is the *single-shooting* method, already treated in section (3.4.1), thanks to its easy implementation and computational cost. This approach leverages the Indirect Methods (IMs) formulation to establish a practical and reproducible methodology capable of navigating the intricate dynamics of the CR3BP. The complete analytical procedure is detailed in the following section.

The set of ODEs to be integrated can be generally described as

$$\dot{\boldsymbol{y}} = \boldsymbol{f}(\boldsymbol{y}(t), t) \tag{3.34}$$

and, since the OCP may also considers some constant values, a new augmented vector $\boldsymbol{z}$ is introduced

$$\boldsymbol{z} = \begin{Bmatrix} \boldsymbol{y}^T \\ \boldsymbol{c}^T \end{Bmatrix} \tag{3.35}$$

where $\boldsymbol{c}$ is a vector that contains all the constants. Hence, the set of ODEs becomes

$$\dot{\boldsymbol{z}} = \frac{d\boldsymbol{z}}{dt} = \boldsymbol{f}(\boldsymbol{z}(t), t) \tag{3.36}$$

where

$$\dot{\boldsymbol{c}} = \frac{d\boldsymbol{c}}{dt} = 0 \tag{3.37}$$

The BCs result fulfilled if

$$\boldsymbol{\chi}(\boldsymbol{z}) = \boldsymbol{0} \tag{3.38}$$

At this point, one has to find the design vector to reach the final state while complying with all the BCs. For this purpose, the implemented *single-shooting* method helps to search the initial vector $\boldsymbol{q}_0^*$ that returns $\boldsymbol{\chi}(\boldsymbol{q}_0) = \boldsymbol{0}$, as seen in section (3.4.1). Considering every initial state variable as unknown, for the most general case, the iterative process starts defining $\boldsymbol{q}_0 = \boldsymbol{z}_0$; the boundary error on the BCs at the *r-th* iteration is then computed as $\boldsymbol{\chi}(\boldsymbol{q}_r)$. The error at the next step is computed via a first order Taylor expansion

$$\boldsymbol{\chi}(\boldsymbol{q}_{r+1}) = \boldsymbol{\chi}(\boldsymbol{q}_r) + \frac{\partial \boldsymbol{\chi}(\boldsymbol{q}_r)}{\partial \boldsymbol{q}_{r+1}}(\boldsymbol{q}_{r+1} - \boldsymbol{q}_r) \tag{3.39}$$

The partial derivatives of the constraint vector $\boldsymbol{\chi}$ with respect to the design vector compose the Jacobian matrix $\boldsymbol{J}$: this is pivotal to understand how to correct the initial guess, hence how to update the design vector $\boldsymbol{q}$.

The following shortening are now introduced

$$\boldsymbol{\chi}_r \triangleq \boldsymbol{\chi}(\boldsymbol{q}_r) \tag{3.40a}$$
$$\boldsymbol{J}(\boldsymbol{\chi}_r) \triangleq \boldsymbol{J}(\boldsymbol{\chi}(\boldsymbol{q}_r), \boldsymbol{q}_{r+1}) \tag{3.40b}$$

If a solution exists, then $\boldsymbol{\chi}_{r+1} = \boldsymbol{0}$, and the iterative solution is rewritten as

$$\boldsymbol{\chi}_r + [\boldsymbol{J}(\chi_r)]\,(\boldsymbol{q}_{r+1} - \boldsymbol{q}_r) = \boldsymbol{0} \tag{3.41}$$

From Equation (3.41) one can compute the design vector at the next step ($r$+1-*th* iteration) as

$$\boldsymbol{q}_{r+1} = \boldsymbol{q}_r - [\boldsymbol{J}(\chi_r)]^{-1}\,\boldsymbol{\chi}_r \tag{3.42}$$

In summary, the OCP in the presented MPBVP aims to find the optimal initial state $\boldsymbol{z}_0^*$ that, evolving following specific ODEs of the dynamical system, reaches the desired final target $\boldsymbol{z}_f^*(\boldsymbol{z}_0^*(t), t)$ while fulfilling the BCs. The ODEs to be integrated are reported in Equation (3.36) and, in a explicit form, in section (3.5). The integrator is based on the Adams-Moulton formulations and implements an implicit multistep numerical method [24].

Furthermore, in order to improve the implemented method and increase the robustness, two different parameters have been added; the first one is a correction factor that reduces the update on the initial vector, thus

$$\boldsymbol{z}_{r+1} = \boldsymbol{z}_r - \kappa_1 \left[\boldsymbol{J}(\chi_r)\right]^{-1} \boldsymbol{\chi}_r \tag{3.43}$$

where $\kappa_1 = 0.001 \div 1$ is the relaxation parameter adopted for the current thesis. Lower values are suitable for the first guess, while when the problem is near to the convergence, higher values are required. The second parameter is added to aid the first steps of the iterative process, allowing the error to increase for a few iteration while it searches for the right descent direction. Hence,

$$\max(\chi_i)_{r+1} < \kappa_2 \cdot \max(\chi_i)_r \tag{3.44}$$

where $\kappa_2 = 2 \div 3$. If the equation does not hold true, a bisection is imposed on the correction $\kappa_1$ up to five times.

## 3.5 OCP for spacecraft trajectory optimisation

Here is reported the set of ODEs subject to optimisation, that represents the spacecraft dynamical system

$$\frac{d\xi}{d\tau} = \dot{\xi} \tag{3.45a}$$

$$\frac{d\eta}{d\tau} = \dot{\eta} \tag{3.45b}$$

$$\frac{d\zeta}{d\tau} = \dot{\zeta} \tag{3.45c}$$

$$\frac{d^2\xi}{d\tau^2} = \xi + 2\dot{\eta} - \frac{1-\mu}{\rho_{13}^3}(\xi + \mu) - \frac{\mu}{\rho_{23}^3}[\xi - (1-\mu)] + \frac{T_\xi}{m} \tag{3.45d}$$

$$\frac{d^2\eta}{d\tau^2} = \eta - 2\dot{\xi} - \frac{1-\mu}{\rho_{13}^3}\eta - \frac{\mu}{\rho_{23}^3}\eta + \frac{T_\eta}{m} \tag{3.45e}$$

$$\frac{d^2\zeta}{d\tau^2} = -\frac{1-\mu}{\rho_{13}^3}z - \frac{\mu}{\rho_{23}^3}z + \frac{T_\zeta}{m} \tag{3.45f}$$

$$\frac{dm}{d\tau} = -\frac{T}{c} \tag{3.45g}$$

It is important to highlight that every quantity in Equations (3.45) is non-dimensional, as previously shown in section (2.3). Furthermore, the last line (3.45g) is subject to the same previous transformation, here presented

$$m = \bar{m}/\bar{m}_0 \tag{3.46a}$$

$$T = \bar{T} \cdot (t^*)^2/(\bar{m}_0 \cdot l^*) \tag{3.46b}$$

$$c = \bar{c} \cdot t^*/l^* \tag{3.46c}$$

where $m$, $T$, $c$ are, respectively, the SC non-dimensional mass, thrust and effective exhaust velocity; their dimensional counterpart is marked with a bar, while $m_0$ is the initial mass and will be treated in Chapter (4).

Equations in (3.45) can be compacted in the following form [25]

$$\frac{d\boldsymbol{\rho}}{d\tau} = \boldsymbol{\mathcal{V}} \tag{3.47a}$$

$$\frac{d\boldsymbol{\mathcal{V}}}{d\tau} = \mathbf{g}(\boldsymbol{\rho}) + \mathbf{h}(\boldsymbol{\mathcal{V}}) + \frac{\boldsymbol{T}}{m} \tag{3.47b}$$

$$\frac{dm}{d\tau} = -\frac{T}{c} \tag{3.47c}$$

where, clearly,

$$\boldsymbol{\rho} = \{\xi \quad \eta \quad \zeta\}^T \tag{3.48a}$$

$$\boldsymbol{\mathcal{V}} = \{\dot{\xi} \quad \dot{\eta} \quad \dot{\zeta}\}^T \tag{3.48b}$$

and

$$\mathbf{g}(\boldsymbol{\rho}) = \begin{Bmatrix} \xi - \dfrac{1-\mu}{\rho_{13}^3}(\xi+\mu) - \dfrac{\mu}{\rho_{23}^3}[\xi - (1-\mu)] \\ \eta - \dfrac{1-\mu}{\rho_{13}^3}\eta - \dfrac{\mu}{\rho_{23}^3}\eta \\ -\dfrac{1-\mu}{\rho_{13}^3}z - \dfrac{\mu}{\rho_{23}^3}z \end{Bmatrix} \tag{3.49a}$$

$$\mathbf{h}(\boldsymbol{\mathcal{V}}) = \begin{Bmatrix} 2\dot{\eta} \\ -2\dot{\xi} \\ 0 \end{Bmatrix} \tag{3.49b}$$

$$\boldsymbol{T} = \{T_\xi \quad T_\eta \quad T_\zeta\}^T \tag{3.49c}$$

The aim of the Optimal Control Theory applied to the set of ODEs in Equations (3.45) is to find the optimal control law $\boldsymbol{u}^*(\tau)$ that maximises the SC final mass. The state vector of the problem $\boldsymbol{x}(\tau) \in \mathbb{R}^n$ is

$$\boldsymbol{x} = \{\xi \quad \eta \quad \zeta \quad \dot{\xi} \quad \dot{\eta} \quad \dot{\zeta} \quad m\}^T \tag{3.50}$$

and for every state variable is defined an associated corresponding adjoint variable, thus an augmented state vector $\boldsymbol{y}(\tau) \in \mathbb{R}^{2n}$ is here defined

$$\boldsymbol{y} = \{\xi \quad \eta \quad \zeta \quad \dot{\xi} \quad \dot{\eta} \quad \dot{\zeta} \quad m \quad \lambda_\xi \quad \lambda_\eta \quad \lambda_\zeta \quad \lambda_{\dot{\xi}} \quad \lambda_{\dot{\eta}} \quad \lambda_{\dot{\zeta}} \quad \lambda_m\}^T \tag{3.51}$$

Regarding the merit index, it is chosen to be the SC mass at the end of the final arc. Adopting the Mayer formulation ($\Phi = 0$), it can be expressed as

$$\mathcal{J} = \varphi = m_f = m_{n_p} \tag{3.52}$$

From the system of ODEs in Equation (3.45) is now possible to explicit the Hamiltonian

$$\begin{aligned} \mathcal{H} = \boldsymbol{\lambda}^T \boldsymbol{f} = \sum_{i=1}^{2n} \lambda_i f_i = \lambda_\xi \dot{\xi} + \lambda_\eta \dot{\eta} + \lambda_\zeta \dot{\zeta} + & \\ + \lambda_{\dot{\xi}} \left[ 2\dot{\eta} + \xi - \frac{1-\mu}{\rho_{13}^3}(\xi + \mu) - \frac{\mu}{\rho_{23}^3}(\xi - 1 + \mu) + \frac{T_\xi}{m} \right] + & \\ + \lambda_{\dot{\eta}} \left[ -2\dot{\xi} + \eta - \frac{1-\mu}{\rho_{13}^3}\eta - \frac{\mu}{\rho_{23}^3}\eta + \frac{T_\eta}{m} \right] + & \\ + \lambda_{\dot{\zeta}} \left[ -\frac{1-\mu}{\rho_{13}^3}\zeta - \frac{\mu}{\rho_{23}^3}\zeta + \frac{T_\zeta}{m} \right] + & \\ - \lambda_m \frac{T}{c} & \end{aligned} \tag{3.53}$$

or, in compact form,

$$\mathcal{H} = \boldsymbol{\lambda}_\rho^T \boldsymbol{\mathcal{V}} + \boldsymbol{\lambda}_\mathcal{V}^T \left( \mathbf{g}(\boldsymbol{\rho}) + \mathbf{h}(\boldsymbol{\mathcal{V}}) + \frac{\boldsymbol{T}}{m} \right) - \lambda_m \frac{T}{c} \tag{3.54}$$

By grouping the thrust terms in Equation (3.54), an alternative form is obtained

$$\mathcal{H} = \boldsymbol{\lambda}_\rho^T \boldsymbol{\mathcal{V}} + \boldsymbol{\lambda}_\mathcal{V}^T \left( \mathbf{g}(\boldsymbol{\rho}) + \mathbf{h}(\boldsymbol{\mathcal{V}}) \right) + \frac{T}{m} \left( \mathcal{S}_\mathcal{F} \right) \tag{3.55}$$

where

$$\mathcal{S}_\mathcal{F} = \boldsymbol{\lambda}_\mathcal{V}^T \frac{\boldsymbol{T}}{T} - \lambda_m \frac{m}{c} \tag{3.56}$$

is the so called *Switching Function.*

In the presented scenario, the control vector $\boldsymbol{u}(\tau)$ is composed by the three terms of the thrust vector $\boldsymbol{T}$ that define its magnitude and direction. As mentioned before, the optimal control law $\boldsymbol{u}^*$ that maximises the merit index in the OCP, is the one that maximises the Hamiltonian in Equation (3.53), in accordance with the PMP.

From Equation (3.55) it can be noticed that the Hamiltonian is linear with respect to the control vector, the thrust: as described in section (3.2.2), in such case a *bang-bang* control law arises. Therefore, the thrust must be maximised when the Switching Function (SF) is positive or nullified when it assumes a negative value. Thus,

$$T = \begin{cases} T_{\max} & \text{if} \quad \mathcal{S}_{\mathcal{F}} > 0 \\ 0 & \text{if} \quad \mathcal{S}_{\mathcal{F}} < 0 \end{cases} \tag{3.57}$$

Focusing on the thrust direction, a useful result can be obtained from Lawden's work [26]: the optimal thrust direction that maximises the SF (and consequently $\mathcal{H}$), is parallel to the adjoint velocity vector $\boldsymbol{\lambda}_{\mathcal{V}}$, called *primer vector*

$$\boldsymbol{\lambda}_{\mathcal{V}} = \begin{Bmatrix} \lambda_{\dot{\xi}} \\ \lambda_{\dot{\eta}} \\ \lambda_{\dot{\zeta}} \end{Bmatrix} \qquad \lambda_{\mathcal{V}} = ||\boldsymbol{\lambda}_{\mathcal{V}}|| \tag{3.58}$$

In Figure (3.3) is shown the thrust vector $\boldsymbol{T}$ and its components in the synodic RF, as seen in section (2.2). Two characteristic angles are thus defined: $\alpha_T$ is the angle between the thrust vector and the $\hat{\boldsymbol{\xi}}$ axis, while $\beta_T$ indicates the elevation with respect to the fundamental $\hat{\boldsymbol{\xi}}$-$\hat{\boldsymbol{\eta}}$ plane.

$$\boldsymbol{T} = \begin{Bmatrix} T_{\xi} \\ T_{\eta} \\ T_{\zeta} \end{Bmatrix} = T \begin{Bmatrix} \cos\beta_T \cos\alpha_T \\ \cos\beta_T \sin\alpha_T \\ \sin\beta_T \end{Bmatrix} \tag{3.59}$$

By deriving the Hamiltonian in Equation (3.54) with respect to the characteristic angles, one can find their optimal value:

$$\frac{\partial \mathcal{H}}{\partial \alpha_T} = -\lambda_{\dot{\xi}} \sin\alpha_T + \lambda_{\dot{\eta}} \cos\alpha_T = 0 \tag{3.60a}$$

$$\frac{\partial \mathcal{H}}{\partial \beta_T} = \lambda_{\dot{\zeta}} \cos\beta_T - (\lambda_{\dot{\eta}} \cos\alpha_T + \lambda_{\dot{\eta}} \sin\alpha_T) \sin\beta_T = 0 \tag{3.60b}$$

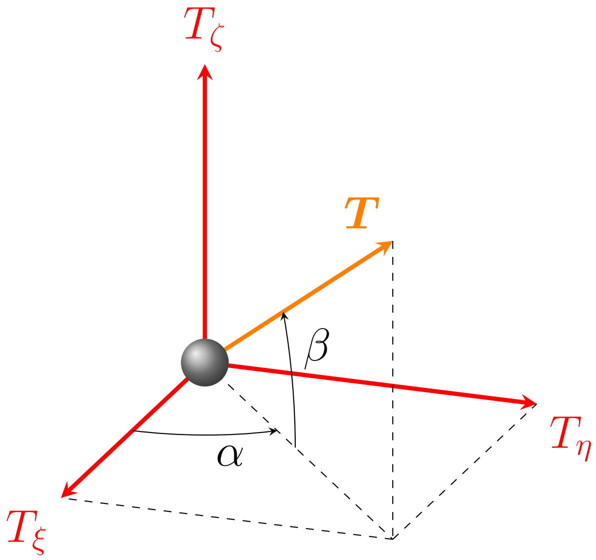

Figure 3.3: Thrust vector

Therefore, the optimal directions are obtained:

$$\cos\alpha_T \cos\beta_T = \frac{\lambda_{\dot{\xi}}}{\lambda_{\mathcal{V}}} \tag{3.61a}$$

$$\sin\alpha_T \cos\beta_T = \frac{\lambda_{\dot{\eta}}}{\lambda_{\mathcal{V}}} \tag{3.61b}$$

$$\sin\beta_T = \frac{\lambda_{\dot{\zeta}}}{\lambda_{\mathcal{V}}} \tag{3.61c}$$

which are the cosine directors of the primer vector itself. Subsequently, the values of the adjoint variables are obtained by integrating the Euler-Lagrange Equations (3.14): their explicit form for the current problem is here omitted, but it can be found in Appendix A.

As described, the problem would be completely defined and could be solved. However, the automatic computation of thrust and coast phases ($\mathcal{S}_\mathcal{F} > 0$ and $\mathcal{S}_\mathcal{F} < 0$, respectively) could be challenged by the complex gravitational interactions that arise from a highly non-linear dynamic system. In fact, numerical problems may occur whether the SF fluctuates around the zero: the correction process described in section (3.4.1) could shift significantly the switching function, eliminating desired arcs or adding new ones. The consequences of this phenomenon are a scarce accuracy for the error gradients and convergence problems, even if this happens in few steps during the correction. Hence, one of the main challenges while using IMs is to handle thrust discontinuities in order to prevent numerical problems in the computation of error gradients: different strategies have been developed to manage it, such as smoothing techniques [27].

In the current thesis, a different approach is adopted. The *switching structure* is defined *a priori* and modified if the PMP is violated: it consists of a sequence of predefined thrust (T) or coast (C) arcs, where the final one is always T, for example [T, C, T, C, T]. At the begin, the simplest coast-thrust sequence is adopted, then modified when required from the PMP.

The trajectory is divided into a sequence of phases, in the same number of the arcs: a MPBVP is, thus, produced. Each *j-th* phase has a duration of $\Delta\tau_j$, subject to optimisation and generally unknown. In addition, the boundary conditions specify that at the switching points (i.e. those that link two adjacent phases) the SF must be null.

The presented problem and solving methods improves the numerical accuracy and speed convergence, compared to other strategies that set the thrust value during integration, according to instantaneous values of the SF.

# 4 Earth-Moon transfer trajectories

In this Chapter are discussed the optimal transfer trajectories deriving from the previously described framework. All the trajectories are computed in the domain of the CR3BP, using the EoM in Chapter (2).

Firstly, the trajectory subject to optimisation is created and the spacecraft defined; secondly, the results for a two-arc sequence are presented, followed by an algorithm to change the structure and a consequent five-arc.

The values presented in the Chapter are non-dimensional, following the procedure described in Section (2.2) and (2.3), unless specified.

## 4.1 Definition of the mission

The problem as described in Chapter (3) is completely defined and ready to be implemented, however, the numerical implementation poses significant challenges. Direct convergence from a Low Earth Orbit (LEO) to the Moon is extremely difficult, due to the high sensitivity of the IMs to initial costate estimates. The computation, in this case, should consider the Earth escape, the transfer phase and the lunar capture: any small perturbation in the presented dynamical system could lead to divergence. For this reason, a base trajectory subject to optimisation is designed, to have a guide in the complex dynamical system and to aid the convergence.

First, however, is presented the concept of the SC, based on ESA's SMART-1 mission [3], the first European SC to travel to and orbit around the Moon with a ion thruster.

### 4.1.1 The spacecraft

This research focuses on the optimisation and analysis of low-thrust lunar transfer trajectories. To achieve the high mass efficiency required for such manoeuvres, EP was selected as the primary propulsion architecture. This choice reflects the significant maturation of EP technologies over the last several decades, offering high specific impulse ($I_{sp}$) that makes deep-space exploration more mass-efficient.

The spacecraft was designed as a 500kg vehicle, allowing for a robust scientific payload and high manoeuvrability during the Earth-Moon transfer trajectory. To fulfil the mission objectives, a thruster based on ArianeGroup's Radio-frequency Ion Thruster (RIT) 10 EVO [28] performance was designed, as the high specific impulse and the nominal thrust provide the necessary efficiency and control to execute the low-thrust transfers proposed in this study.

The fundamental performance parameters, including initial mass, thrust, specific impulse, and effective exhaust velocity, are detailed in Table (4.1). These values are presented alongside their corresponding non-dimensional forms, derived through Equations (3.46a) to (3.46c).

| Dimensional form | | | Adimensional form | |
|---|---|---|---|---|
| $\bar{m}_0$ | 500.00 | kg | $m_0$ | 1.00 |
| $\bar{m}_{\text{dry}}$ | 350.00 | kg | $m_{\text{dry}}$ | 0.70 |
| $\bar{T}$ | 0.01 | N | $T$ | 7.32 |
| $\bar{I}_{\text{sp}}$ | 3000.00 | s | | |
| $\bar{c}$ | 29.43 | km/s | $c$ | 28.72 |

Table 4.1: Spacecraft's data

### 4.1.2 Base trajectory

As mentioned before, it would be very difficult to find a direct solution from LEO to the Moon, due to the implemented methods. A low-thrust trajectory could take up to months to be completed and the accurate research of the initial costates that bring to the desired final target results challenging. To help the convergence, a base trajectory has been computed: once this framework is defined, one can start from one of its points and proceed with the optimisation. Once the first solution has been found, the optimal solution can be propagated back in time and the work becomes easier. This is the actual process implemented in the presented thesis.

To design the base trajectory, three fundamental considerations were made: the problem is planar, the SC shall start in LEO and it shall terminate its path in the translunar environment. The first assumption is the most relevant, as it slims the problem and aids the convergence, since 2 states and 2 costates are considered null. Hence, the state vector $\boldsymbol{x}$ becomes

$$\boldsymbol{x} = \left\{\xi \quad \eta \quad \dot{\xi} \quad \dot{\eta} \quad m\right\}^T \tag{4.1}$$

and the augmented one, $\boldsymbol{y}$, that considers also the costates

$$\boldsymbol{y} = \left\{\xi \quad \eta \quad \dot{\xi} \quad \dot{\eta} \quad m \quad \lambda_\xi \quad \lambda_\eta \quad \lambda_{\dot{\xi}} \quad \lambda_{\dot{\eta}} \quad \lambda_m\right\}^T \tag{4.2}$$

while the out-of-plane angle $\beta$ in Equations (3.61a) to (3.61c) is null and constant. The second assumption takes into account a realistic scenario where the SC is released in a cheaper orbit, with respect to higher ones, while the other provides the right conditions to perform the optimisation.

With these assumptions, the base trajectory is computed as a Edelbaum transfer, as described in section (2.4.2), starting from an altitude of 500km above Earth's surface. The SC fires continuously in the tangential direction of its orbit, increasing slowly its energy, until a sufficient energy level that allows to travel to the Moon is reached. For this manoeuvre, the estimated value for the Jacobi constant in Equation (2.33) is 2.742618355: such value is enough to explore any region of the binary system and will be later decreased to capture the Moon and be bounded in a narrow region.

Table (4.2) shows the initial and final conditions of the base trajectory, where $\varphi$ is the initial angle between $\hat{\boldsymbol{\xi}}_S$-axis and the SC's position vector for the Earth escape. The computed trajectory in the synodic RF is shown in Figures (4.1) and (4.3), while Figure (4.2) reports the evolution of the Jacobi constant over time ($\tau$). As one can observe, while the SC increases the energy of its orbit, $\mathcal{J}_C$ decreases its value until it reaches the target, then remains constant; the thrust phase lasts approximately $\Delta\tau = 0.712$, where the mass goes from $m_0 = 1.0000$ to $m = 0.8183$. Hence, the fuel consumption for the whole manoeuvre is $m_p = 0.18161216$: later will be shown that this represents the quasi totality of the propellant needed to perform the trajectory.

| | Initial state | Final state |
|---|---|---|
| $\tau$ | 0.00000000 | 1.75399642 |
| $\xi$ | 0.00155611 | 0.99771504 |
| $\eta$ | 0.01150128 | −0.00022492 |
| $\dot{\xi}$ | −4.77618217 | −0.52288978 |
| $\dot{\eta}$ | 5.69203227 | −1.54866914 |
| $m$ | 1.00000000 | 0.81838784 |
| $\varphi$ | 0.69813170 | - |
| $\mathcal{J}_C$ | 55.23215161 | 2.74261835 |

Table 4.2: Base trajectory: initial and final state

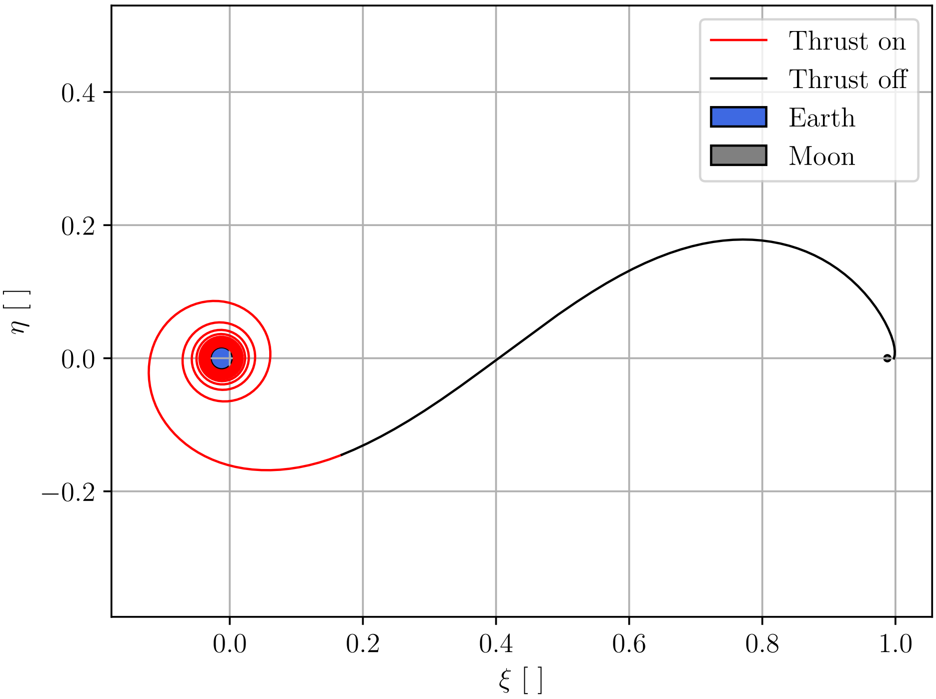

Figure 4.1: Base trajectory

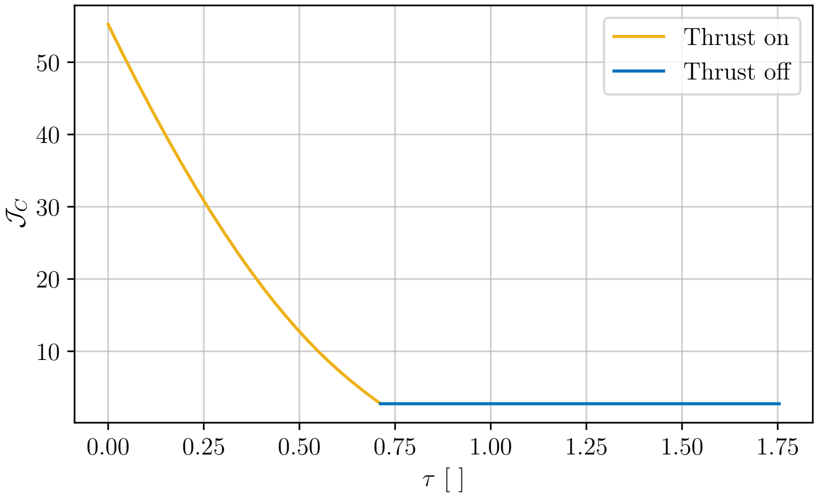

Figure 4.2: $\mathcal{J}_C$ over time

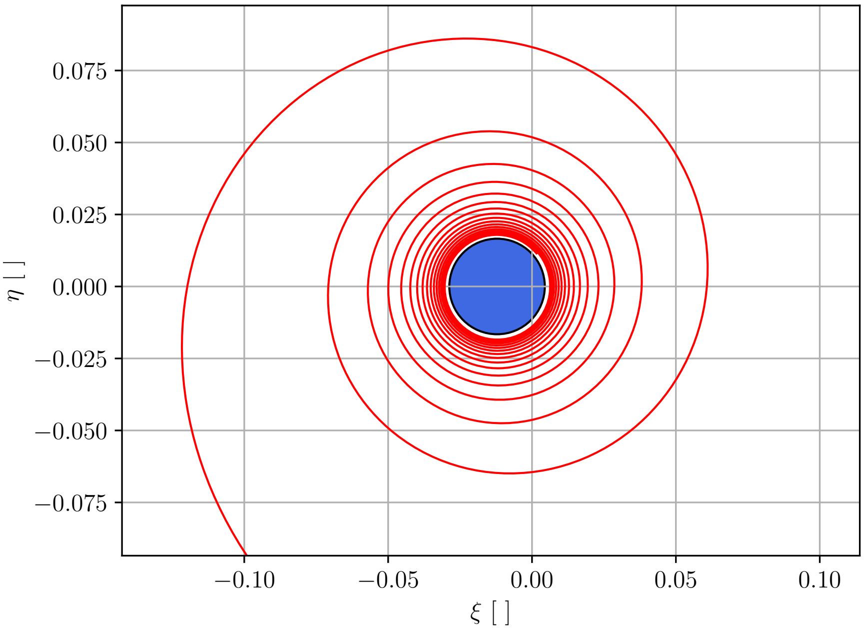

(a) Zoom on Earth

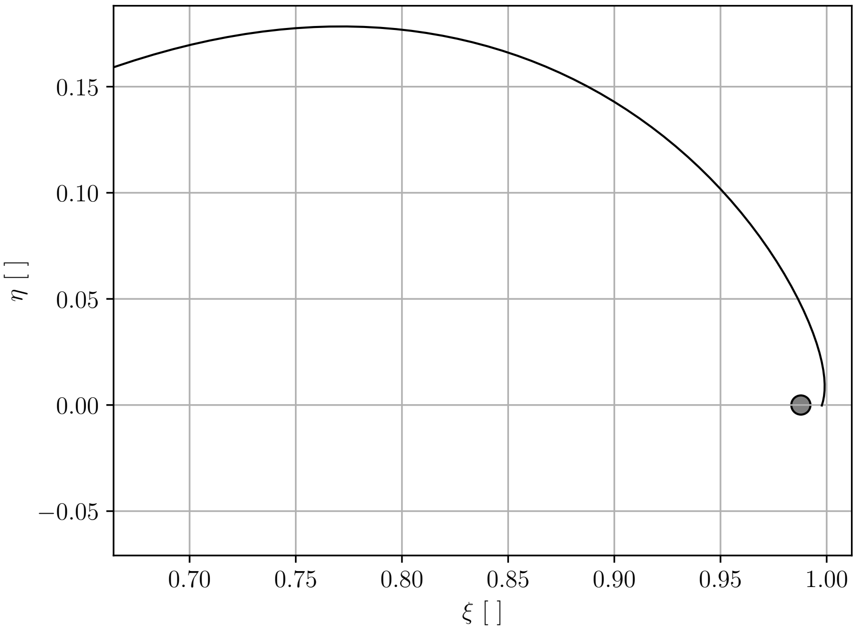

(b) Zoom on the Moon

Figure 4.3: Zoom on the primaries within the base trajectory

## 4.2 Two-arc trajectory

This section presents the primary foundational result of the current research. By implementing the optimal control framework detailed in Chapter (3), the analysis aims to identify a fundamental optimal solution to serve as a robust baseline for more complex manoeuvres. Specifically, the trajectory is composed of two predefined phases: a Coast (C) arc and a Thrust (T) arc. The SC performs a Moon capture and lays on a high-elliptical orbit around the natural satellite.

The section first outlines the boundary conditions of such problem, at the initial and terminal points, then evaluates the results of the optimisation.

### 4.2.1 Initial conditions

The difficulties that arise for a direct convergence from LEO to the Moon have led to the design of a base trajectory, useful to start the optimisation process. The most sensitive segments are the escape from Earth and the Moon capture, characterised by high-intensity gravitational gradients. Within this study, the optimisation focuses exclusively on the lunar arrival phase, while the Earth departure is modelled as the already presented Edelbaum escape.

For the scope of this research, an internal point of the base trajectory is taken as a reference state for the initial conditions. Specifically, such point is taken from the intermediate deep-space phase, where the influence of both primaries is comparable. In the CR3BP domain, the gravitational interactions of the primaries on the SC can lead to unexpected solutions, so the selected state represents an adequate start for the optimisation, as it does not preclude any result.

The specific point, defined as $\mathcal{P}_{\text{mid}}$, is established on the base trajectory at $\tau = 1.3$. At this epoch, the SC has just begun its approach to the Moon in the synodic RF. The state vector of the spacecraft at this point is presented in Table (4.3): as from now, the initial time $\tau_0 = 0$ of the optimal trajectory is referred as starting from $\mathcal{P}_{\text{mid}}$, unless specified.

| State in $\mathcal{P}_{\text{mid}}$ | | | |
|---|---|---|---|
| $\tau$ | 1.30000000 | $m$ | 0.81838784 |
| $\xi$ | 0.77415337 | $\dot{\xi}$ | 0.65280333 |
| $\eta$ | 0.17837035 | $\dot{\eta}$ | −0.00669083 |

Table 4.3: Initial conditions for the two-arc trajectory

Furthermore, the OCP formulated in the previous Chapter requests to set an initial guess for the costate variables in Equation (4.2). This initialisation represents one of the main challenges that IMs pose, as costates lack direct physical intuition and their magnitudes can vary significantly depending on the problem scaling. In addition to this, they are extremely sensitive and, for a model like the CR3BP, even small perturbations can lead to radically different trajectories. As detailed in Chapter (3), in fact they govern the path's evolution by determining when thrust is required, via the SF, and in which direction, as per Equations (3.61a) to (3.61c).

For this research, to identify a viable initial guess for the costate vector, and to familiarise with their influence on the trajectory, a trial and error process was implemented. This process aimed to comprehend the appropriate magnitude and sign, approaching the desired target, while satisfying the boundary conditions. The velocity adjoints revealed to be like a combination of pedals and steering wheel in a vehicle [12]: the magnitude indicates how relevant is the corresponding state at the same moment, while the sign implies the use of the accelerator (thrust along the current direction for positive values) or brakes (thrust in the opposite direction for negative values). The combination of the two velocity adjoint variables return the thrust direction, considering the relevance of the variable by its magnitude. The position adjoint variables, on the other hand, express the importance of change for the associated state. For this specific problem, the magnitude revealed to range between $10^{-1}$ to $10^{-3}$.

Furthermore, the switching structure was defined a priori as a sequence of a Coast (C) and a Thrust (T) arc: this represents the most simple case, where the SC waits to get to the Moon and, at the right time, decreases the velocity to capture it. Therefore, the SF was required to remain negative for a specified duration before transitioning to a positive value until the terminal state is reached.

Within this domain, the raw guess is here reported

$$\tilde{\boldsymbol{\lambda}}_0 = \begin{Bmatrix} \tilde{\lambda}_\xi \\ \tilde{\lambda}_\eta \\ \tilde{\lambda}_{\dot{\xi}} \\ \tilde{\lambda}_{\dot{\eta}} \\ \tilde{\lambda}_m \end{Bmatrix} = \begin{Bmatrix} -0.060000000 \\ 0.030000000 \\ -0.002500000 \\ 0.026000000 \\ 0.998000000 \end{Bmatrix} \tag{4.3}$$

while the switching times have been set to decrease the SC's velocity enough to capture the Moon; since two arcs have been implemented, two times are required, $\tau_1$ to transition from Coast (C) to Thrust (T) and $\tau_f$ to determine the end of the trajectory. Hence,

$$\tilde{\boldsymbol{\tau}} = \begin{Bmatrix} \tilde{\tau}_1 \\ \tilde{\tau}_f \end{Bmatrix} = \begin{Bmatrix} 0.440000 \end{Bmatrix} \tag{4.4}$$

Since all the initial state variables are fixed, the *shooting method* implemented updates only the adjoint variables and the two switching times, aiming to find the initial vector $\boldsymbol{y}_0^*$ that evolves in time to reach the desired state $\boldsymbol{y}_f^*$ while satisfying the BCs $\boldsymbol{\chi}(\boldsymbol{y}) = \mathbf{0}$.

### 4.2.2 Terminal conditions

To close the IM formulation, a set of BCs must be satisfied at final time. These ensure that the trajectory reaches the desired state while fulfilling the optimality conditions in Equations (3.13a) to (3.13d).

The target state vector $\boldsymbol{x}_t$ has been defined to aid the convergence, as many others were adopted unsuccessfully due to the simplicity of the switching structure. The objective is to capture the Moon, hence the target is identified as a point on the $\hat{\boldsymbol{\xi}}_S$-axis in the cislunar environment, while the velocity is set to be enough low to stay in orbit. The final mass is subject to optimisation, thus it does not appear in the target state vector; the values are reported in Table (4.4).

| State | Target value |
|---|---:|
| $\xi$ | 0.96396485 |
| $\eta$ | $-0.00203904$ |
| $\dot{\xi}$ | $-0.10002013$ |
| $\dot{\eta}$ | 0.45135373 |

Table 4.4: Target for the two-arc trajectory

For what concerns the optimality conditions, according to the schema in Figure (3.1), if a state variable is not strictly constrained at the final time, the corresponding costate must be null at the same time, otherwise it is free and can assume any value. The initial state vector fixes the five variables, hence no condition arise. On the other hand, the target state vector only fixed position and velocity variables, leaving the final mass subject to optimisation. Therefore, an optimal condition arise from Equation (3.13d):

$$(\lambda_m)_f = 1 \tag{4.5}$$

while all the other costates are free.

Another constraint is derived from the definition of a MPBVP. The switching function must assume a null value when transitions from an arc to another: in this specific two-arc trajectory, the only constraint is

$$\mathcal{S}_{\mathcal{F}}(\tau_1) = 0 \tag{4.6}$$

As a result, considering $*_f$ a final value and $*_t$ a target, the boundary conditions to be fulfilled for the optimal trajectory are

$$\boldsymbol{\chi}(\boldsymbol{y}) = \begin{Bmatrix} \mathcal{S}_{\mathcal{F}}(\tau_1) \\ \xi_f - \xi_t \\ \eta_f - \eta_t \\ \dot{\xi}_f - \dot{\xi}_t \\ \dot{\eta}_f - \dot{\eta}_t \\ (\lambda_m)_f - 1 \end{Bmatrix} = \mathbf{0} \tag{4.7}$$

### 4.2.3 Results

The resultant optimal two-arc trajectory was computed using the iterative process described in Section (3.4.1). Initially, the relaxation parameter $\kappa_1$ in Equation (3.43) was set to 0.001 to aid the research of the minimum; once the solution was sufficiently close to convergence, $\kappa_1$ was updated to 0.01. This phased approach ensured numerical stability while pursuing a high-precision solution.

The *shooting method* updated the initial costate variables $\boldsymbol{\lambda}_0^*$ and switching time $\boldsymbol{\tau}^*$ vectors through successive iterations, providing, in the end, the following values

$$\boldsymbol{\lambda}_0^* = \begin{Bmatrix} \lambda_\xi^* \\ \lambda_\eta^* \\ \lambda_{\dot{\xi}}^* \\ \lambda_{\dot{\eta}}^* \\ \lambda_m^* \end{Bmatrix} = \begin{Bmatrix} -0.060025446 \\ 0.029957750 \\ -0.002515295 \\ 0.025987403 \\ 0.976695999 \end{Bmatrix} \tag{4.8}$$

$$\boldsymbol{\tau}^* = \begin{Bmatrix} \tau_1^* \\ \tau_f^* \end{Bmatrix} = \begin{Bmatrix} 0.44198700 \\ 0.4980000 \end{Bmatrix} \tag{4.9}$$

The implemented indirect method successfully converged on an optimal trajectory that evolves from $\boldsymbol{y}_0^*$ to $\boldsymbol{y}_f^*$ providing the optimal control law and fulfilling the boundary conditions. Indeed, the terminal violation of the BCs, represented by the norm of $\boldsymbol{\chi}(\boldsymbol{y})$ at the end of the computation is

$$||\boldsymbol{\chi}(\boldsymbol{y})|| = 6.46 \cdot 10^{-7} \tag{4.10}$$

Specifically, the error for the position states $\xi$ and $\eta$ was reduced to the order of $10^{-8}$: in dimensional terms, it corresponds to a position accuracy within a few meters. The evolution of the position and velocity states is illustrated in

Figure (4.4). For visual clarity, coasting arcs are represented by blue or black lines and thrust phases by orange segments in the plots presented below.

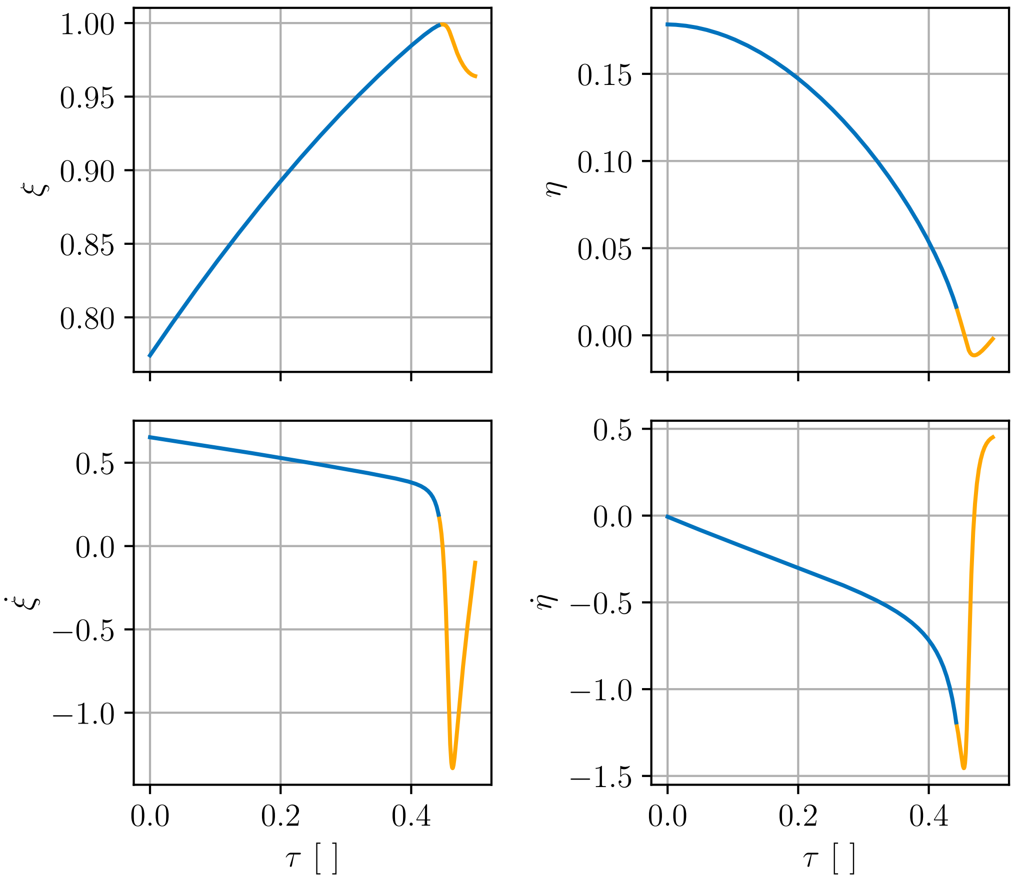

Figure 4.4: Evolution of $\xi$, $\eta$, $\dot{\xi}$ and $\dot{\eta}$ over time

The resulting optimal trajectory in the synodic RF is shown in Figure (4.5). The SC follows the baseline path from $\mathcal{P}_{\text{mid}}$ to $\boldsymbol{x}(\tau_1)$, where the thruster is turned on to start the manoeuvre. Therefore, the first arc consists if an unpowered coast, while the second controls the path. During this terminal phase, the SC has to perform a deceleration manoeuvre to capture the Moon. The entire trajectory is completed in approximately 52 hours (2.16 days, corresponding to $\tau_f = 0.498$), of which 6 hours are spent in a continuous thrusting phase.

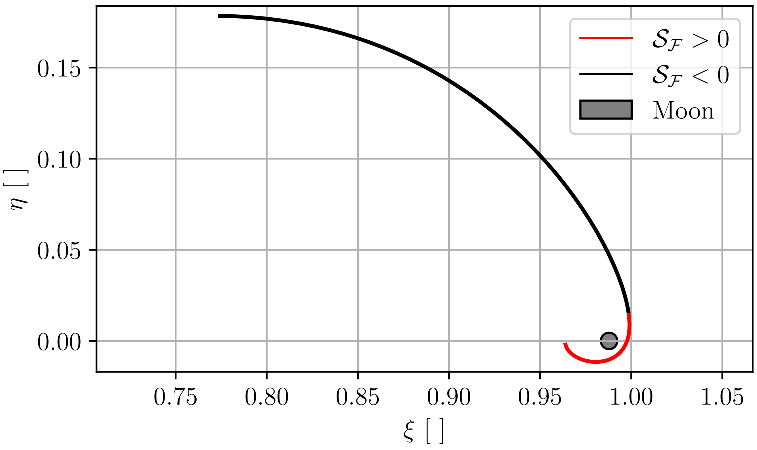

Figure 4.5: Two-arc optimal trajectory in synodic RF

Throughout the first unpowered arc, the Jacobi constant remains invariant, as per Equation (2.33). Its initial value, $(J_C)_0 = 2.74261835$, corresponds to an energy level that allows the spacecraft to reach every point of the binary Earth-Moon system, meaning that, without active control, it would escape the Moon after a brief fly-by. On the other hand, as shown in Figure (4.6), during thrust arc $\mathcal{J}_C$ is increased due to the effect of the thruster: the aim was to transition from the initial value $(J_C)_0$ to a lower energy level that could enclose the SC in a region nearby the Moon. Indeed, the final value $(J_C)_f = 3.75331196$ closes the Zero Velocity Curves around the natural satellite, providing a circular-shaped region of possible motion and ensuring the lunar capture.

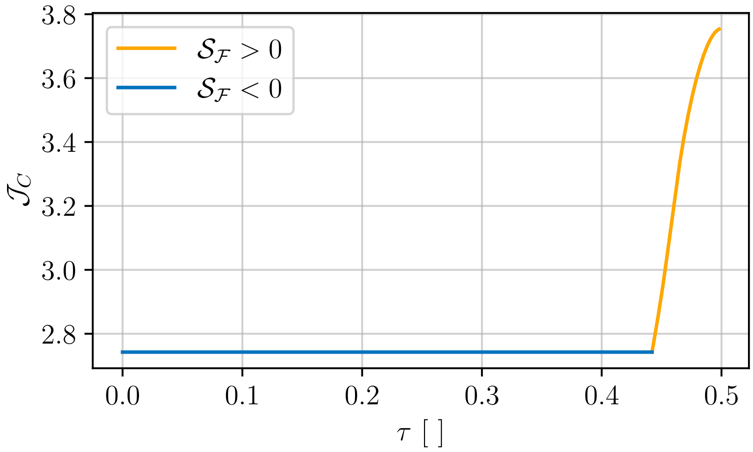

Figure 4.6: Evolution of $\mathcal{J}_C$ over time

The costate vector defined in (4.8) evolves over time according to the Euler-Lagrange equations in Appendix A (Figure 4.7). These variables constitute the foundation of the optimal control law that permits to lead the SC from its initial state to the target, while satisfying all the BCs. Specifically, the costates shape the switching function $\mathcal{S}_{\mathcal{F}}$, deciding when the thrust is required and define the optimal thrust vector direction throughout the powered arc.

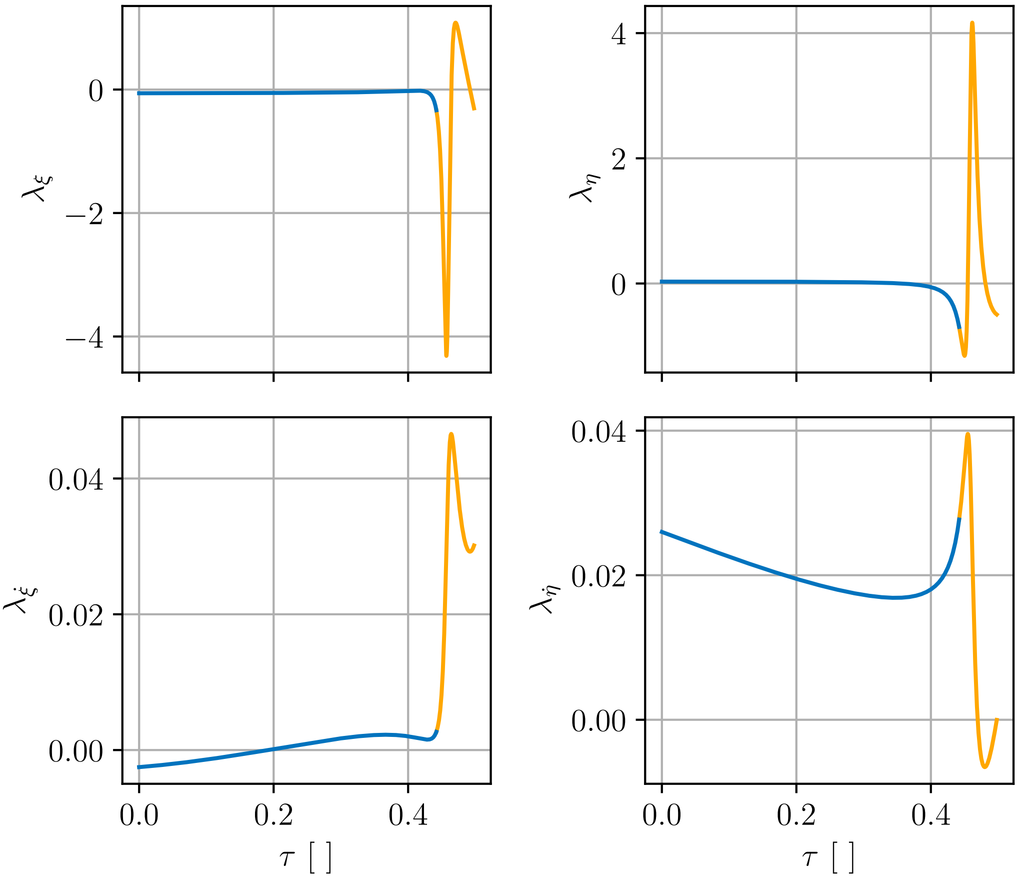

Figure 4.7: Evolution of position and velocity costates over time

The switching function, as per Equation (3.56), is computed and illustrated in Figure (4.8). In accordance with the predefined two-arc structure, the SF remains negative during the coasting phase, nullifies at the switching point $\tau_1$ and finally switches to positive values guiding the thrust arc. Since a *bang-bang* control law is implemented in the present research, the thrust is independent of the SF's instant magnitude: only its sign is relevant, governing the control that is either null or $T_{\max}$, according to the PMP.

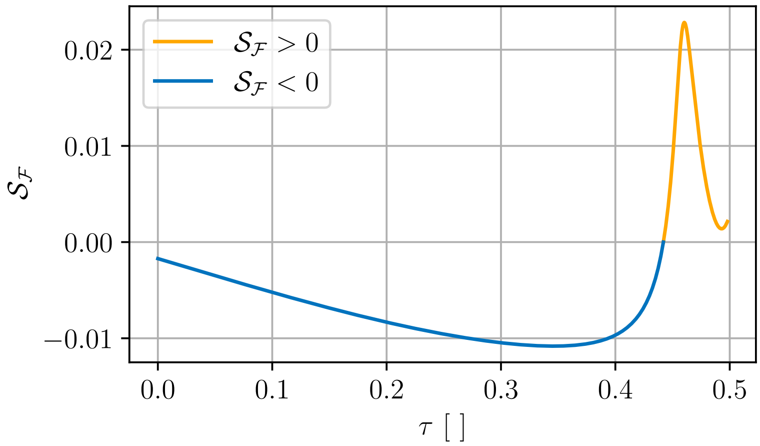

Figure 4.8: Switching function $\mathcal{S}_\mathcal{F}$ over time

Furthermore, the optimal thrust direction is derived from Equations (3.61a) to (3.61c) imposing the out-of-plane angle $\beta = 0$. As expected, given the state of the SC at $\tau_1$, it initially fires quasi tangentially to the trajectory to decrease the velocity. The direction then evolves to obtain the desired result (Figure 4.9). This underscores the fundamental role of the costate vector that guide the state towards the optimal solution, computing when thrust is required and in which direction.

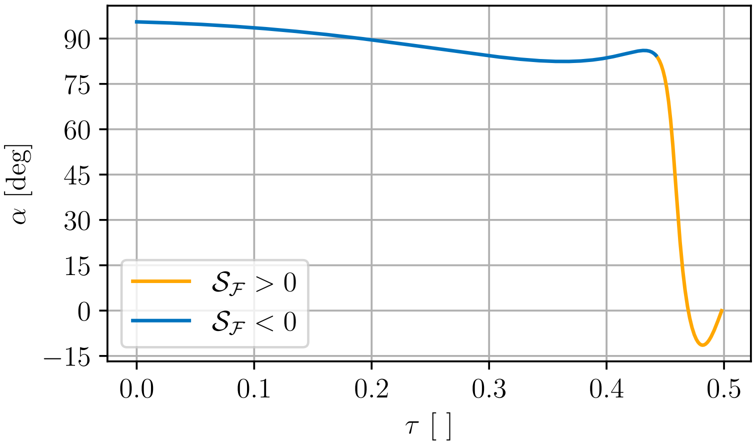

Figure 4.9: In-plane thrust angle $\alpha$ over time

The aim of the optimisation, however, focuses on the final mass. In particular, the trajectory has to be performed minimising the propellant consumption, thus having the maximum final mass, as expressed in the merit index. The initial mass at ($\tau_0$) is set to $m_0 = 0.81838784$, as a consistent part of the available fuel has already been used to perform the escape from Earth. At this point, the mass has a discontinuous evolution: from $\tau_0$ in $\mathcal{P}_{\text{mid}}$ to the ignition point $\tau_1$ it remains constant, then decreases during the second arc in accordance to Equation (3.45g). The resulting final mass is

$$m_f = 0.80410574 \tag{4.11}$$

indicating that, for the lunar capture manoeuvre, approximately 7.14 kg of propellant are required. The associated costate $\lambda_m$ increases monotonically throughout the trajectory, according to Equation (A.2g), assuming a final unit value with a precision of $\approx 10^{-7}$, consistent with the optimality condition. Figure (4.10) shows the evolution of the mass and the costate associated over time.

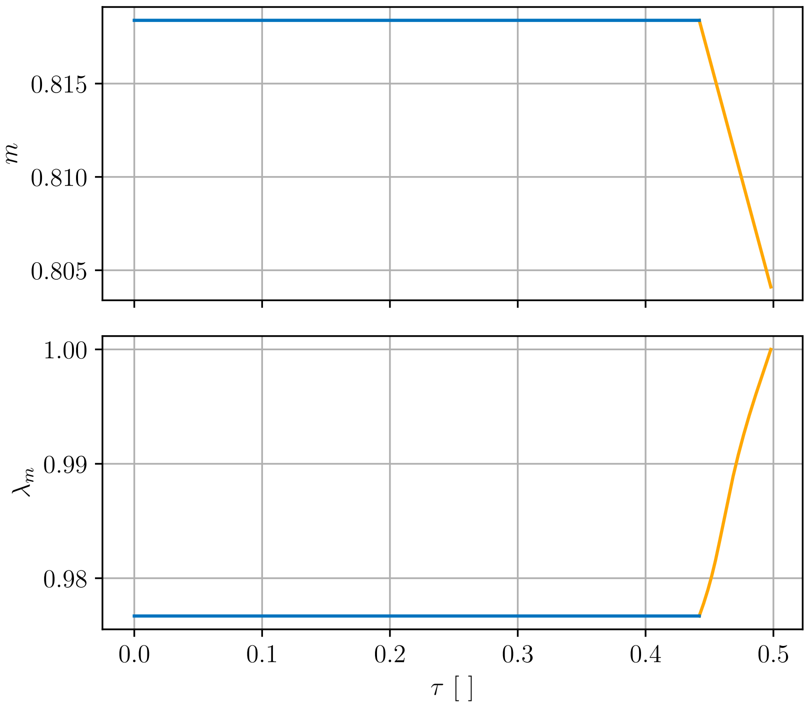

Figure 4.10: Mass $m$ and mass costate $\lambda_m$ evolution over time

To verify the effectiveness of the capture manoeuvre, the final state $y_f^*$ is used as the initial condition for a long-term propagation. This step ensures that the spacecraft remains in a stable lunar orbit without the need for further active control. The trajectory is propagated for five additional orbital periods in a complete unpowered motion ($T = 0$), as illustrated in Figure (4.11).

In the synodic RF the spacecraft maintains a stable highly-elliptical retrograde orbit around the Moon. This orbital persistence confirms that the energy level achieved during the thrust arc, represented by the final Jacobi Constant $(JC)_f$, is sufficient to prevent escape through the $L_1$ or $L_2$ gateways. The orbit has a period $\mathcal{T} = 0.1074$ (almost 10.7 hours) and throughout the five revolutions the altitude remains within a range of 0.0054 to 0.02422, demonstrating that the indirect method optimisation successfully performed a viable lunar capture.

A notable feature of the resulting trajectory is its apparent apsidal precession within the synodic frame. Specifically, the orbit exhibits a clockwise rotation of its major axis. This phenomenon is a direct consequence of the rotating reference frame: the line of apsides appears to recess in the direction opposite to the binary system's motion due to transport velocity. With each revolution, the orbit shifts by approximately 6°, completing a full rotation and returning to its original orientation relative to the Earth-Moon line after one sidereal month ($\tau = 2\pi$).

Crucially, the Jacobi Constant remains invariant during this phase, ensuring that the precession occurs within a bounded region and that the spacecraft remains gravitationally bound without the risk of an autonomous escape.

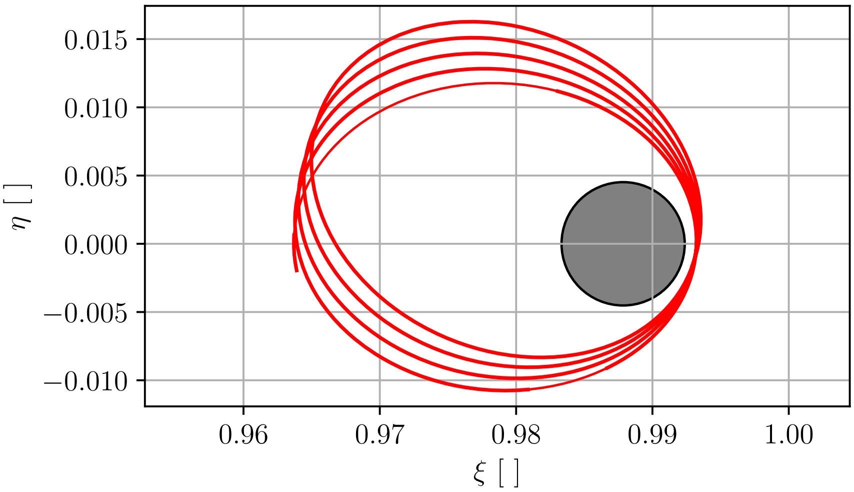

Figure 4.11: Propagation of the optimal two-arc trajectory

## 4.3 Five-arc trajectory

The main challenge in IMs lies in the initialisation of the optimisation process. Identifying a suitable set of initial costates is difficult and can take several tries before getting something useful. However, once a single solution is obtained, its costate vector serves as a reference, facilitating the research of trajectories with slightly different boundary conditions: this process is defined *costate continuation*.

While the two-arc solution successfully demonstrated lunar capture, certain terminal conditions remained inaccessible under that specific control structure. During the exploration of the costate space, several candidate trajectories emerged where the SF indicated the need for additional thrusting intervals. Because the switching structure was defined a priori, these cases violated the necessary conditions of PMP. To cope with this, an algorithm was implemented to modify the switching structure where necessary.

This section describes how the previous result was used as reference to reach a circular lunar orbit, describing the update algorithm, the new boundary conditions and the resulting five-arc trajectory.

### 4.3.1 Structure change algorithm

Working with IMs requires the satisfaction of several condition to ensure the optimal solution. One of these is the PMP, that states that the optimal control vector $\boldsymbol{u}^* \in \mathcal{U}$ must maximise the Hamiltonian per each point in the desired trajectory.

For the implemented OCP, the Hamiltonian is linear with respect to the thrust; consequently, the control must be maximum ($T_{\max}$) when $\mathcal{S}_{\mathcal{F}} > 0$ and null otherwise. When convergence is achieved, it results necessary to verify if the PMP is respected, namely that the SF matches the assumed switching structure. In the case a violation occurs, the trajectory results *sub-optimal*, and a change in strategy has to be implemented.

For this case, part of the IMAGE (Indirect Method Automated Global Exploration) (Figure 4.12) extracted from Mascolo's work [12] is used to transform a sub-optimal solution into an optimal. This represents an algorithm designed for low-thrust trajectories research using IMs: a complete description can be found in his work.

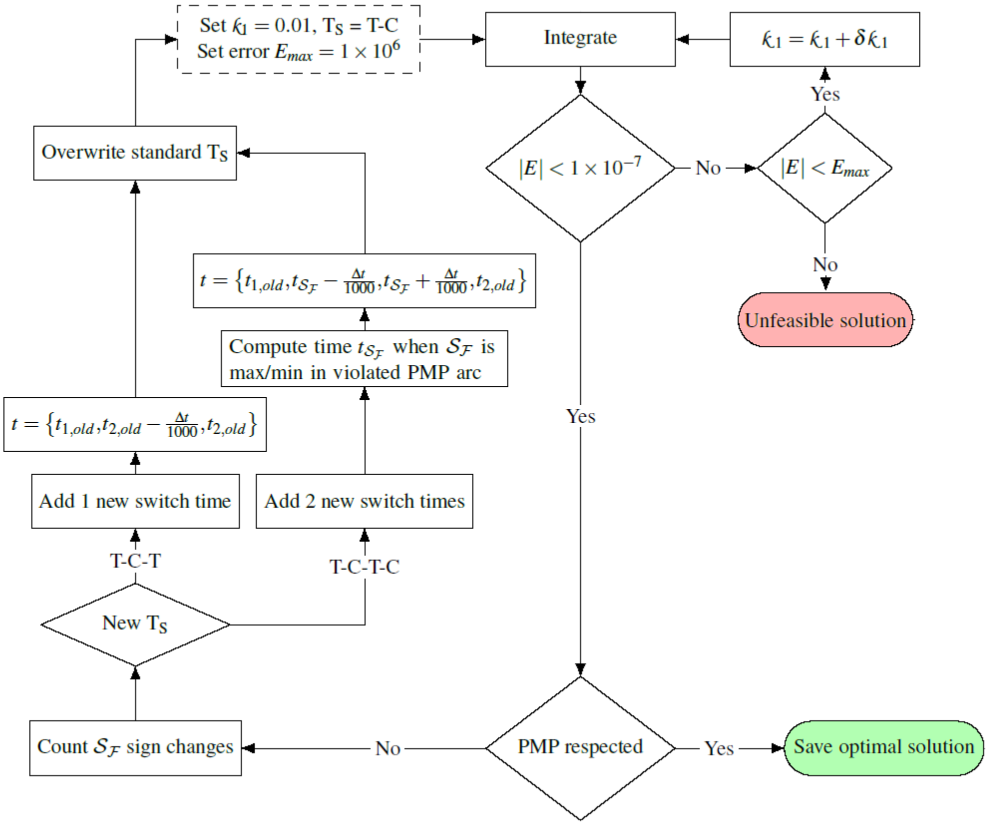

Figure 4.12: Part of IMAGE algorithm [12]

In the presented Figure (4.12) is shown the case where one or two arcs are added, but the code can also remove thrust phases if required. When one is added, automatically an interior point is located at the most appropriate position. If it is needed at the end, the algorithm includes a very short burn time just before $\tau = \tau_f$. In the case a thrust phase is required in the middle of a coasting phase, the selected midpoint is the one where the SF assumes the maximum or minimum value in the violated arc; thus, two switching times are inserted. At the end of the process, the switching structure gets updated and the integration process restarts, trying to fit the new arcs and converge while respecting the PMP.

Following the described procedure, the previous two-arc solution has been modified to satisfy other boundary conditions. In particular, during the research for other solutions, a new thrust phase was suggested at the begin of the trajectory, while the last thrust arcs has been split by a coast phase. Hence, the resultant solution is a five-arc optimal trajectory.

### 4.3.2 Initial conditions

The research for an improved solution led to the development of the five-arc trajectory detailed in this section. Modifying the costate vector from the previous reference solution, the SF was reshaped and three more arcs were added: an initial thrust segments and a coast-thrust sequence at the end. Consequently, the switching structure was updated to [T-C-T-C-T].

For this reason, the initial conditions for the optimal trajectory were adjusted relative to the base trajectory described in section (4.1.2). In particular, the new set of initial states is set for $\tau = 1.2$, in $\mathcal{P}'_{\text{mid}}$ (Table 4.5): this time extension was necessary to observe the effect of the first thrust phase on the solution.

| State in $\mathcal{P}_{\text{mid}}{}'$ | | | |
|---|---|---|---|
| $\tau$ | 1.20000000 | $m$ | 0.81838784 |
| $\xi$ | 0.70582691 | $\dot{\xi}$ | 0.71447974 |
| $\eta$ | 0.17095491 | $\dot{\eta}$ | 0.15786921 |

Table 4.5: Initial conditions for the five-arc trajectory

The initial costate vector $\boldsymbol{\lambda}_0$ is derived from the previous result in (4.8). These values were modified to reshape the SF into a five-arc profile, aiming to aid the convergence. Since this represents a different problem, the following values represent a guess for the shooting method:

$$\tilde{\boldsymbol{\lambda}}_0 = \begin{Bmatrix} \tilde{\lambda}_\xi \\ \tilde{\lambda}_\eta \\ \tilde{\lambda}_{\dot{\xi}} \\ \tilde{\lambda}_{\dot{\eta}} \\ \tilde{\lambda}_m \end{Bmatrix} = \begin{Bmatrix} -0.055025000 \\ 0.029957700 \\ -0.003000000 \\ 0.028987400 \\ 0.976700000 \end{Bmatrix} \tag{4.12}$$

Subsequently, the time vector $\boldsymbol{\tau} \in \mathbb{R}^5$ is defined. A small value is assigned for the first thrust arc and the second coast phase; in this way the trajectory remains close to the previous one at the begin of the iterative process:

$$\tilde{\boldsymbol{\tau}} = \begin{Bmatrix} \tilde{\tau}_1 \\ \tilde{\tau}_2 \\ \tilde{\tau}_3 \\ \tilde{\tau}_4 \\ \tilde{\tau}_f \end{Bmatrix} = \begin{Bmatrix} 0.001000 \\ 0.538000 \\ 0.600000 \\ 0.614000 \\ 0.643000 \end{Bmatrix} \tag{4.13}$$

### 4.3.3 Terminal conditions

Considering a scientific-based mission, the objective is to reach a stable orbit around the Moon, where the SC can operate or start further manoeuvres such as low-altitude descent or lunar landing. For this reason, the target is a circular orbit with an altitude of 2000 km.

The final state is set in the translunar environment, on the $\hat{\boldsymbol{\xi}}_S$ axis of the synodic RF (Table 4.6). For a circular orbit, in such point the velocity is purely along the $\hat{\boldsymbol{\eta}}_S$-axis and can be approximated as

$$\mathcal{V}_c = -\sqrt{\frac{\mu_2}{r_{23}}} \cdot \frac{t^*}{l^*} \tag{4.14}$$

The negative sign is assigned to denote the retrograde lunar orbit.

| State | Target value |
|---|---:|
| $\xi$ | 0.97812777 |
| $\eta$ | 0.00000000 |
| $\dot{\xi}$ | 0.00000000 |
| $\dot{\eta}$ | −1.11798540 |

Table 4.6: Target for the five-arc trajectory

Following the two-arc trajectory scenario, the initial and final state variables are fixed, leaving their corresponding costate free. The only exception is the final mass, subject to optimisation, that again leads to the condition in (4.5). However, now the switching function must satisfy four different constraints:

$$\mathcal{S}_{\mathcal{F}}(\tau_1) = \mathcal{S}_{\mathcal{F}}(\tau_2) = \mathcal{S}_{\mathcal{F}}(\tau_3) = \mathcal{S}_{\mathcal{F}}(\tau_4) = 0 \tag{4.15}$$

Consequently, the boundary condition vector $\boldsymbol{\chi}(\boldsymbol{y})$ to be satisfied for the optimal trajectory is

$$\boldsymbol{\chi}(\boldsymbol{y}) = \left\{ \begin{matrix} \mathcal{S}_{\mathcal{F}}(\tau_1) \\ \mathcal{S}_{\mathcal{F}}(\tau_2) \\ \mathcal{S}_{\mathcal{F}}(\tau_3) \\ \mathcal{S}_{\mathcal{F}}(\tau_4) \\ \xi_f - \xi_t \\ \eta_f - \eta_t \\ \dot{\xi}_f - \dot{\xi}_t \\ \dot{\eta}_f - \dot{\eta}_t \\ (\lambda_m)_f - 1 \end{matrix} \right\} = \mathbf{0} \tag{4.16}$$

### 4.3.4 Results

The research for the optimal solution followed the previous strategy: at the begin, the relaxation parameter was set to 0.001, then increased to 0.01 as the trajectory was sufficiently close to convergence. The iterative process successfully led to the identification of the initial costate and switching time vectors

$$\boldsymbol{\lambda}_0^* = \begin{Bmatrix} \lambda_\xi^* \\ \lambda_\eta^* \\ \lambda_{\dot{\xi}}^* \\ \lambda_{\dot{\eta}}^* \\ \lambda_m^* \end{Bmatrix} = \begin{Bmatrix} -0.052800950 \\ 0.013142729 \\ -0.001709887 \\ 0.027213385 \\ 0.955484800 \end{Bmatrix} \tag{4.17}$$

$$\boldsymbol{\tau}^* = \begin{Bmatrix} \tau_1^* \\ \tau_2^* \\ \tau_3^* \\ \tau_4^* \\ \tau_f^* \end{Bmatrix} = \begin{Bmatrix} 0.002742956 \\ 0.535052534 \\ 0.619939407 \\ 0.640532624 \\ 0.641249665 \end{Bmatrix} \tag{4.18}$$

This set of costates provides the optimal control law that evolves the initial state $\boldsymbol{y}_0^*$ to the desired target $\boldsymbol{y}_f^*$. Indeed, the boundary conditions are completely respected, yielding a residual of

$$||\boldsymbol{\chi}(\boldsymbol{y})|| = 9.93 \cdot 10^{-7} \tag{4.19}$$

In Figure (4.13) is illustrated the evolution of the position and velocity states during the entire trajectory.

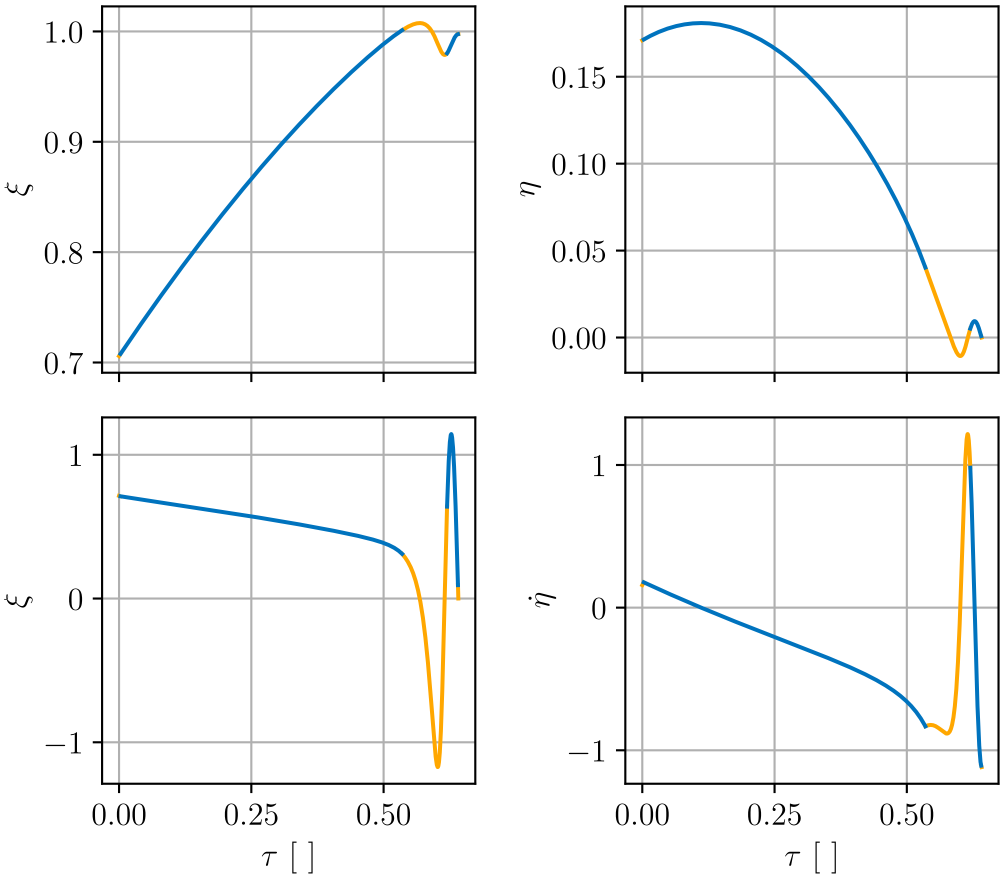

Figure 4.13: Evolution of position and velocity states over time

As illustrated in Figure (4.14), the trajectory performs a complete revolution around the Moon before concluding the capture. The path followed deviates from the baseline, as the initial arc, albeit brief, slightly modifies it. Nevertheless, similarly to the two-arc trajectory, the lunar approach remains ballistic, without any active control. When the SC is in close proximity to the Moon, the thruster initiates the T-C-T sequence to reach the target state. The total flight time is 67 hours, including 9.2 hours of active propulsion.

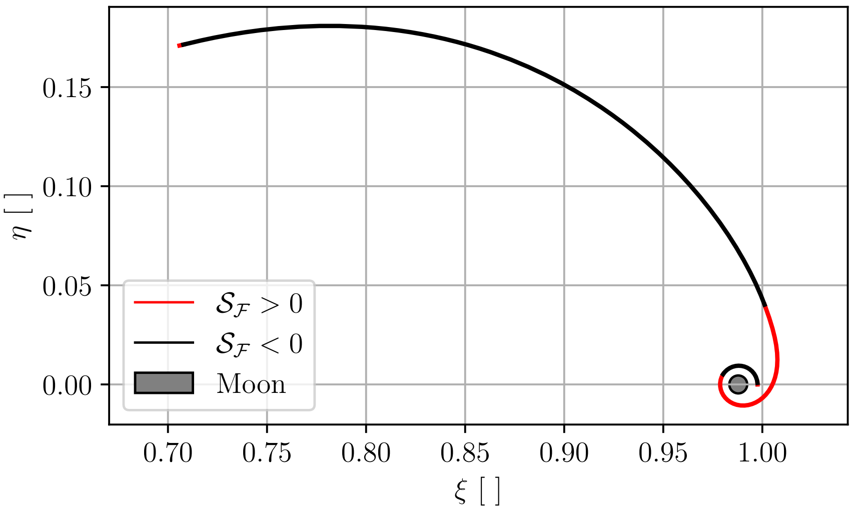

Figure 4.14: Five-arc trajectory in the synodic reference frame

The evolution of the Jacobi constant is discontinuous over time. During the coasting arcs its value is conserved, but it changes when the thrust is active. In Figure (4.15) this profile is evident: the intermediate thrust arc performs a significant deceleration raising the $\mathcal{J}_C$ to 4.21592. This lower energy level confines the spacecraft to a tighter region around the Moon, with respect to the previous solution. The remaining two thrust arcs perform corrective manoeuvres, increasing slightly the energy level at the begin and end of the trajectory.

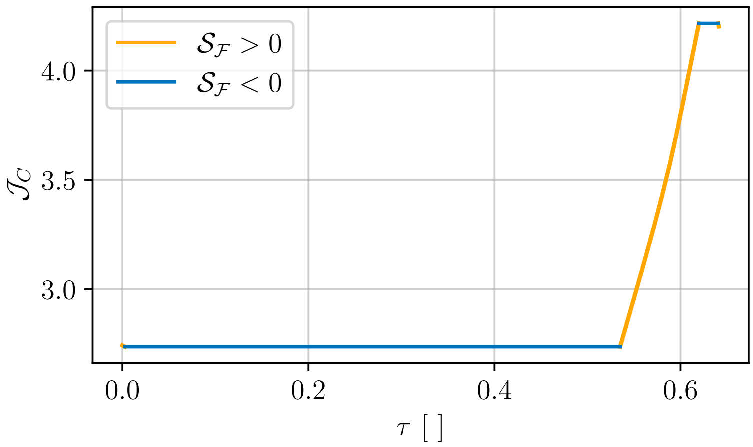

Figure 4.15: $\mathcal{J}_C$ over time - five-arc trajectory

The costate evolution, in Figure (4.16), shapes the SF, leading to a perfect match with the predefined switching structure. In comparison with Figure (4.8), one can observe that five-arc $\mathcal{S}_{\mathcal{F}}$ is an effective extension of the two-arc profile (Figure 4.17). The perturbations applied to the initial costates provided the right sequence of positive and negative values, generating a thrust arc on the "tail" and a coast arc that splits the final manoeuvres. The current structure satisfies completely the PMP and no further structural modification is required.

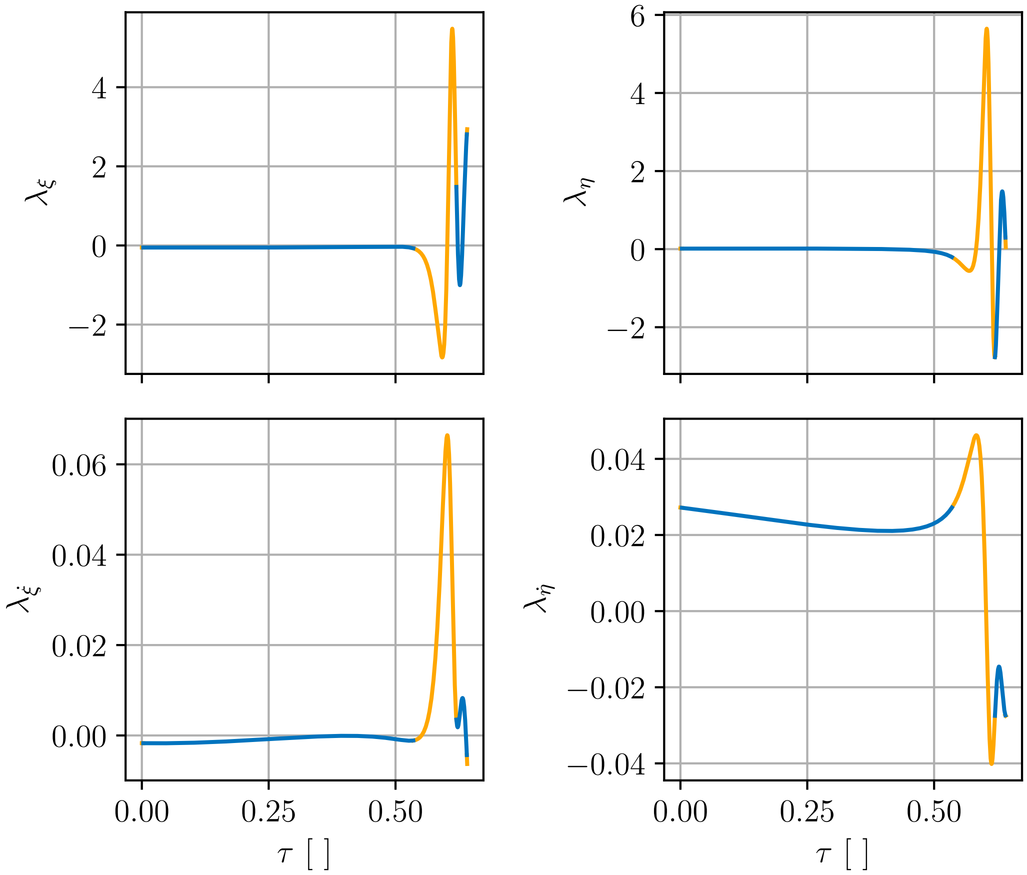

Figure 4.16: Evolution of position and velocity costates over time

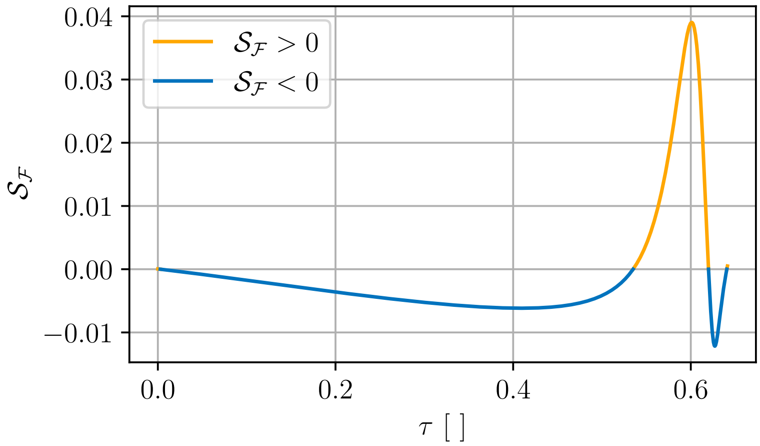

Figure 4.17: Switching function for the five-arc trajectory

The analysis on the in-plane thrust angle (Figure 4.18) confirms that the intermediate manoeuvre has the expected behaviour: the SC fires opposite to its velocity vector to decrease the magnitude. As regards the other two thrust arcs, they correct the trajectory aligning it with the circularity constraints.

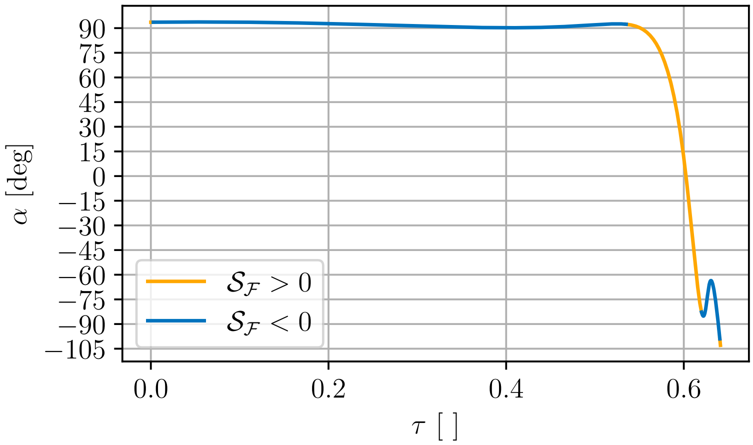

Figure 4.18: In-plane thrust angle $\alpha$ over time

The increased complexity of the target resulted in higher propellant consumption. Specifically, the continuous thrust consumed 11.24 kg of propellant, as the final optimal mass is

$$m_f = 0.7958960860 \tag{4.20}$$

The evolution of the mass and its corresponding costate, once again respect the discontinuity of the thrust during the trajectory, as illustrated in Figure (4.19). They both remain constant during the coasting phase, while the mass decreases and the costate increases during powered arcs. The final value for the costate is unitary with a precision in the order of $10^{-8}$, respecting the condition in Equation (4.5).

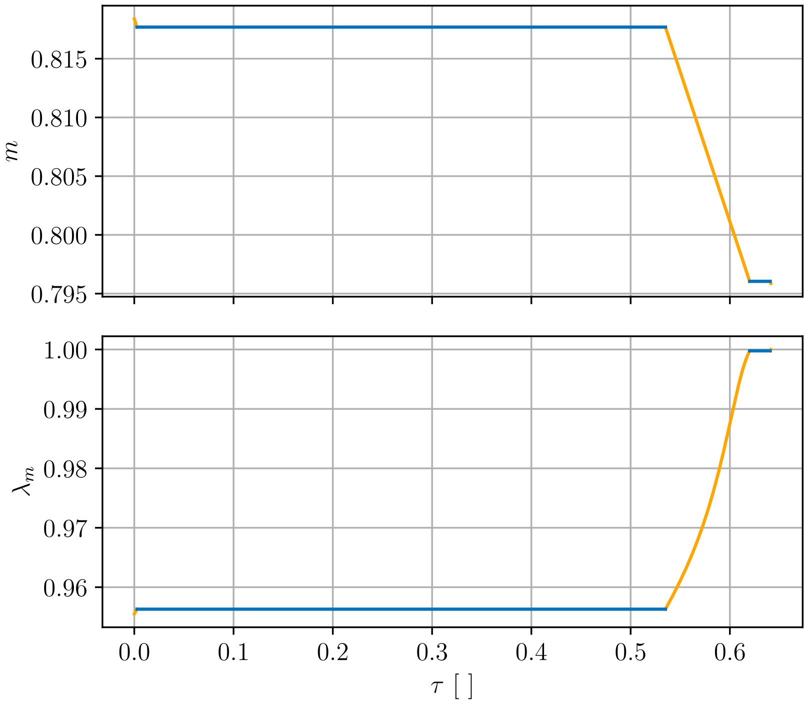

Figure 4.19: Mass and its corresponding costate over time

In the end, an analysis of the resulting orbit is performed. Propagating the final conditions $\boldsymbol{y}_f$ for five revolutions, one can observe the main characteristics of the orbit, presented in Figure (4.20). The geometry matches the desired circular orbit: specifically, the SC oscillates in an range between 3737 and 3603 km from the Moon's centre. In a two-body approximation, considering a Keplerian orbit, this corresponds to an eccentricity of

$$e = \frac{r_a - r_p}{r_a + r_p} = 0.01966 \tag{4.21}$$

This value is below the minimum lunar orbit eccentricity, considered negligible in the CR3BP. Finally, the orbit has a period $\mathcal{T} = 0.0531$, or 5.4 hours, approximately half of the previous case.

In conclusion, the 5-arc solution identifies an optimal capture trajectory that successfully transitions the spacecraft into a stable, quasi-circular motion around the Moon. While the propellant cost is marginally higher than the 2-arc capture, the resulting 2000 km circular orbit provides superior operational utility for a scientific mission.

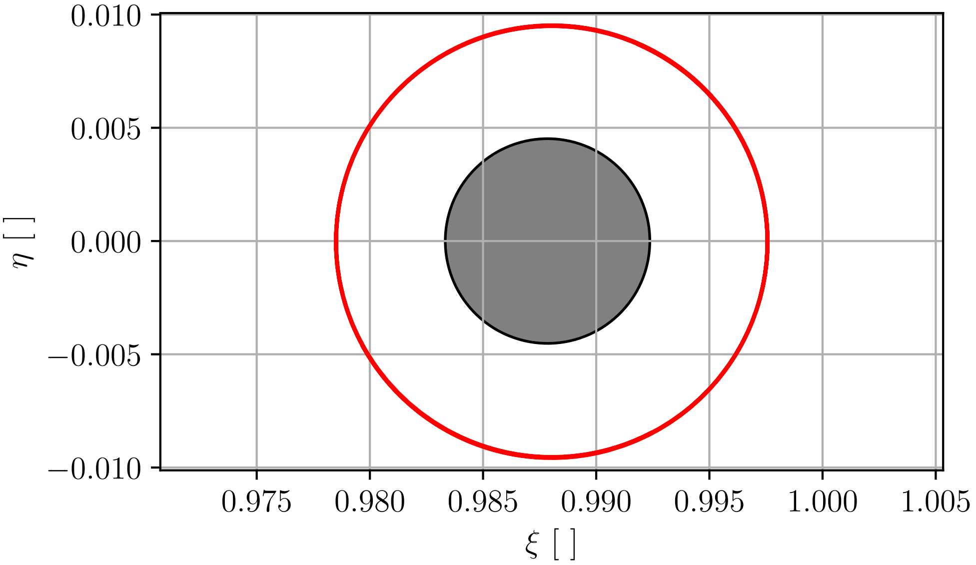

Figure 4.20: Propagation of the five-arc trajectory

# 5 | Conclusions

This thesis focused on the optimisation of low-thrust Earth-Moon transfer trajectories within the planar CR3BP. Driven by the scientific objectives of the current space sector, this research successfully modelled transfers that minimise propellant consumption. The resulting stable orbits can be exploited as a operational platform or a starting point for subsequent manoeuvres.

The core of this work relied on the implementation of IMs to solve the defined OCP. While IMs are notably sensitive and less intuitive than direct methods, they provided the mathematical insights necessary to ensure solution optimality while maintaining high robustness and low computational cost.

The optimisation was framed as a MPBVP and solved using a shooting method. The aim was to maximise the final mass, hence minimise the propellant consumption and allow the SC to have more space for the scientific payload. During the study, some sub-optimal solutions were found, leading to the modification of the switching structure to respect the PMP.

The resultant control law for the implemented OCP was a *bang-bang* type. This particular law is governed by the costates evolution over time, that shape the switching function and direct the thrust vector. Hence, the costates guided the trajectory. Additionally, to aid the convergence, a base Earth-Moon trajectory was computed, consisting in a Edelbaum escape, a deep-space phase and a lunar approach. Only the two latter were subject to optimisation, targeting first a Moon capture, then a circularisation of the orbit.

In conclusion, the objectives of this research have been successfully fulfilled. The implemented code serves as a robust and computationally efficient baseline for identifying mass-effective trajectories within the Earth-Moon binary system. The two-arc solution represented a baseline to more complex multi-burn structures, overcoming the convergence sensitivities typically associated with the initialisation of IMs. Indeed, with minimal additional effort, a more practical five-arc trajectory ending in a circular orbit has been computed. In the context of the present Lunar Renaissance, these results offer a versatile basis for further mission-specific investigations.

*"I learned a lot, by the end of everything.*
*The past is past, now, but that's... you know, that's okay! It's never really gone completely. The future is always built on the past, even if we won't get to see it. Still, it's, um, time for something new, now."*
- Riebeck

# Bibliography

[1] Museo Galilei. *Galileo Galilei: Drawings of the Moon, November-December 1609.* URL: `https://brunelleschi.imss.fi.it/galileopalazzostrozzi/object/GalileoGalileiDrawingsOfTheMoon.html`.

[2] Caraveo P. *Conquistati dalla Luna: Storia di un'attrazione senza tempo.* Raffaello Cortina Editore, 2019.

[3] European Space Agency. *SMART-1.* URL: `https://www.esa.int/Science_Exploration/Space_Science/SMART-1/SMART-1_overview`.

[4] China National Space Administration. *Chang'e 3.* 2013. URL: `https://www.nssdc.ac.cn/nssdc_en/html/task/change3.html`.

[5] National Aeronautics and Space Administration. *Artemis Program.* URL: `https://www.nasa.gov/humans-in-space/artemis/`.

[6] Zhang J., Yu H., and Dai H. "Overview of Earth-Moon Transfer Trajectory Modeling and Design". In: *Computer Modeling in Engineering & Sciences* (2022).

[7] Kluever C. *Space Flight Dynamics.* John Wiley & Sons, Incorporated, 2018.

[8] NASA - Jet Propulsion Laboratory. URL: `https://ssd.jpl.nasa.gov/astro_par.html`.

[9] Wakker K.F. *Fundamentals of Astrodynamics.* Institutional Repository Library, Delft, 2015.

[10] Ross S. et al. *Dynamical Systems, the Three-Body Problem and Space Mission Design.* 2022.

[11] Szebehely V. *Theory of orbits: the restricted problem of three bodies.* Academic Press, 1967.

[12] Mascolo L. "Low-Thrust Optimal Escape Trajectories from Lagrangian Points and Quasi-Periodic Orbits in a High-Fidelity Model". PhD thesis. Politecnico di Torino, 2023.

[13] Lagrange J.-L. *Essai sur le Problème des Trois Corps.* 1772.

[14] National Aeronautics and Space Administration. *James Webb Space Telescope*. URL: `https://science.nasa.gov/mission/webb/`.

[15] European Space Agency. *Gaia*. URL: `https://www.esa.int/Science_Exploration/Space_Science/Gaia`.

[16] European Space Agency. *Euclid*. URL: `https://www.esa.int/Science_Exploration/Space_Science/Euclid`.

[17] Archinal B. A. et al. “Report of the IAU Working Group on Cartographic Coordinates and Rotational Elements: 2015”. In: *Celestial Mechanics and Dynamical Astronomy* (2018).

[18] Goebel D. M. and Katz I. *Fundamentals of electric propulsion: Ion and hall thrusters.* John Wiley & Sons, Incorporated., 2008.

[19] De Ruiter A., Damaren C., and Forbes J. *Spacecraft Dynamics and Control. An Introduction.* John Wiley & Sons, 2013.

[20] Betts John T. *Practical Methods for Optimal Control and Estimation Using Nonlinear Programming (2nd Edition).* Society for Industrial and Applied Mathematics (SIAM), 2010.

[21] NASA. *GMAT - General Mission Analysis Tool.* URL: `https://software.nasa.gov/software/GSC-19097-1`.

[22] Ansys. *STK - Systems Tool Kit.* URL: `https://www.ansys.com/it-it/products/missions/ansys-stk`.

[23] Morante D., Sanjurjo Rivo M., and Soler M. “A Survey on Low-Thrust Trajectory Optimization Approaches”. In: *Aerospace* (2021).

[24] Shmpine L. and Gordon M. *Computer Solution of Ordinary Differential Equations: the Initial Value Problem.* San Francisco : W. H. Freeman, 1975.

[25] C. Zhang, Topputo F., and Zhao Yu-Shan. “Low-Thrust Minimum-Fuel Optimization in the Circular Restricted Three-Body Problem”. In: *Journal of Guidance, Control, and Dynamics* (2015).

[26] Lawden D.F. *Optimal Trajectories for Space Navigation.* Butterworths, 1963.

[27] Bertrand R. and Epenoy R. “New smoothing techniques for solving bang-bang optimal control problems”. In: *Optimal Control Applications and Methods* (2002).

[28] ArianeGroup. *RIT Thruster Family Performance Data.* URL: `https://satcatalog.s3.amazonaws.com/components/916/SatCatalog_-_ArianeGroup_-_RIT_2X_-_Datasheet.pdf?lastmod=20210710015151`.

# A | Euler-Lagrange equations for the adjoint variables

$$\dot{\boldsymbol{\lambda}} = -\frac{\partial \mathcal{H}}{\partial \boldsymbol{x}} \tag{A.1}$$

$$\begin{aligned}
\dot{\lambda}_\xi = &-\lambda_{\dot{\xi}} \left[1 - \frac{1-\mu}{\rho_{13}^3} + \frac{3(1-\mu)(\xi+\mu)^2}{\rho_{13}^5} - \frac{\mu}{\rho_{23}^3} + \frac{3\mu(\xi-(1-\mu))^2}{\rho_{23}^5}\right] + \\
&- \lambda_{\dot{\eta}} \left[\frac{3(1-\mu)(\xi+\mu)\eta}{\rho_{13}^5} + \frac{3\mu(\xi-(1-\mu))\eta}{\rho_{23}^5}\right] + \\
&- \lambda_{\dot{\zeta}} \left[\frac{3(1-\mu)(\xi+\mu)\zeta}{\rho_{13}^5} + \frac{3\mu(\xi-(1-\mu))\zeta}{\rho_{23}^5}\right]
\end{aligned} \tag{A.2a}$$

$$\begin{aligned}
\dot{\lambda}_\eta = &-\lambda_{\dot{\xi}} \left[\frac{3(1-\mu)(\xi+\mu)\eta}{\rho_{13}^5} + \frac{3\mu(\xi-(1-\mu))\eta}{\rho_{23}^5}\right] + \\
&- \lambda_{\dot{\eta}} \left[1 - \frac{1-\mu}{\rho_{13}^3} + \frac{3(1-\mu)\eta^2}{\rho_{13}^5} - \frac{\mu}{\rho_{23}^3} + \frac{3\mu\eta^2}{\rho_{23}^5}\right] + \\
&- \lambda_{\dot{\zeta}} \left[\frac{3(1-\mu)\eta\zeta}{\rho_{13}^5} + \frac{3\mu\eta\zeta}{\rho_{23}^5}\right]
\end{aligned} \tag{A.2b}$$

$$\begin{aligned}\dot{\lambda}_\zeta = &-\lambda_{\dot{\xi}}\left[\frac{3(1-\mu)(\xi+\mu)\zeta}{\rho_{13}^5}+\frac{3\mu(\xi-(1-\mu))\zeta}{\rho_{23}^5}\right]+\\ &-\lambda_{\dot{\eta}}\left[\frac{3(1-\mu)\eta\zeta}{\rho_{13}^5}+\frac{3\mu\eta\zeta}{\rho_{23}^5}\right]+\\ &-\lambda_{\dot{\zeta}}\left[-\frac{1-\mu}{\rho_{13}^3}+\frac{3(1-\mu)\zeta^2}{\rho_{13}^5}-\frac{\mu}{\rho_{23}^3}+\frac{3\mu\zeta^2}{\rho_{23}^5}\right]\end{aligned} \tag{A.2c}$$

$$\dot{\lambda}_{\dot{\xi}} = -\lambda_\xi - 2\lambda_{\dot{\eta}} \tag{A.2d}$$

$$\dot{\lambda}_{\dot{\eta}} = -\lambda_\eta + 2\lambda_{\dot{\xi}} \tag{A.2e}$$

$$\dot{\lambda}_{\dot{\zeta}} = -\lambda_\zeta \tag{A.2f}$$

$$\dot{\lambda}_m = \frac{T}{m^2}\lambda_v \tag{A.2g}$$